



AFRL-RQ-WP-TR-2016-0010

**HIGH IMPACT TECHNOLOGY COMPACT
COMBUSTION (HITCC) COMPACT CORE
TECHNOLOGIES**

Andrew W. Caswell

**Combustion Branch
Turbine Engine Division**

**JANUARY 2016
Interim Report**

Approved for public release; distribution unlimited.

See additional restrictions described on inside pages

STINFO COPY

**AIR FORCE RESEARCH LABORATORY
AEROSPACE SYSTEMS DIRECTORATE
WRIGHT-PATTERSON AIR FORCE BASE, OH 45433-7541
AIR FORCE MATERIEL COMMAND
UNITED STATES AIR FORCE**

NOTICE AND SIGNATURE PAGE

Using Government drawings, specifications, or other data included in this document for any purpose other than Government procurement does not in any way obligate the U.S. Government. The fact that the Government formulated or supplied the drawings, specifications, or other data does not license the holder or any other person or corporation; or convey any rights or permission to manufacture, use, or sell any patented invention that may relate to them.

This report was cleared for public release by the USAF 88th Air Base Wing (88 ABW) Public Affairs Office (PAO) and is available to the general public, including foreign nationals.

Copies may be obtained from the Defense Technical Information Center (DTIC)
(<http://www.dtic.mil>).

AFRL-RQ-WP-TR-2016-0010 HAS BEEN REVIEWED AND IS APPROVED FOR
PUBLICATION IN ACCORDANCE WITH ASSIGNED DISTRIBUTION STATEMENT.

*//Signature//

ANDREW W. CASWELL
Program Engineer
Combustion Branch
Turbine Engine Division

//Signature//

CHARLES J. CROSS, Branch Chief
Combustion Branch
Turbine Engine Division
Aerospace Systems Directorate

This report is published in the interest of scientific and technical information exchange, and its publication does not constitute the Government's approval or disapproval of its ideas or findings.

*Disseminated copies will show “//Signature//” stamped or typed above the signature blocks.

REPORT DOCUMENTATION PAGE					Form Approved OMB No. 0704-0188	
<p>The public reporting burden for this collection of information is estimated to average 1 hour per response, including the time for reviewing instructions, searching existing data sources, gathering and maintaining the data needed, and completing and reviewing the collection of information. Send comments regarding this burden estimate or any other aspect of this collection of information, including suggestions for reducing this burden, to Department of Defense, Washington Headquarters Services, Directorate for Information Operations and Reports (0704-0188), 1215 Jefferson Davis Highway, Suite 1204, Arlington, VA 22202-4302. Respondents should be aware that notwithstanding any other provision of law, no person shall be subject to any penalty for failing to comply with a collection of information if it does not display a currently valid OMB control number. PLEASE DO NOT RETURN YOUR FORM TO THE ABOVE ADDRESS.</p>						
1. REPORT DATE (DD-MM-YY) January 2016		2. REPORT TYPE Interim		3. DATES COVERED (From - To) 29 January 2014 – 29 January 2016		
4. TITLE AND SUBTITLE HIGH IMPACT TECHNOLOGY COMPACT COMBUSTION (HITCC) COMPACT CORE TECHNOLOGIES				5a. CONTRACT NUMBER In-house		
				5b. GRANT NUMBER		
				5c. PROGRAM ELEMENT NUMBER 62203F		
6. AUTHOR(S) Andrew W. Caswell				5d. PROJECT NUMBER 3048		
				5e. TASK NUMBER N/A		
				5f. WORK UNIT NUMBER Q1AP		
7. PERFORMING ORGANIZATION NAME(S) AND ADDRESS(ES) Combustion Branch (AFRL/RQTC) Turbine Engine Division Air Force Research Laboratory, Aerospace Systems Directorate Wright-Patterson Air Force Base, OH 45433-7541 Air Force Materiel Command, United States Air Force				8. PERFORMING ORGANIZATION REPORT NUMBER AFRL-RQ-WP-TR-2016-0010		
9. SPONSORING/MONITORING AGENCY NAME(S) AND ADDRESS(ES) Air Force Research Laboratory Aerospace Systems Directorate Wright-Patterson Air Force Base, OH 45433-7541 Air Force Materiel Command United States Air Force				10. SPONSORING/MONITORING AGENCY ACRONYM(S) AFRL/RQTC		
				11. SPONSORING/MONITORING AGENCY REPORT NUMBER(S) AFRL-RQ-WP-TR-2016-0010		
12. DISTRIBUTION/AVAILABILITY STATEMENT Approved for public release; distribution unlimited.						
13. SUPPLEMENTARY NOTES PA Case Number: 88ABW-2016-0506; Clearance Date: 08 Feb 2016.						
14. ABSTRACT <p>During the past fiscal year, researchers with the Air Force Research Laboratory's Combustion Branch made substantial progress in numerous areas including: 1) ultra-compact combustors, 2) inter-turbine burner concepts, 3) bluff-body stabilized turbulent flames, 4) well-stirred reactors for chemical kinetics, and 5) detonation-stabilized turbulent flames. Lean blowout data was collected on propane and jet fuel bluff-body stabilized flames and was combined with data taken from past literature to create a database of over 1,100 data points.</p> <p>The best correlation for the overall dataset included pressure, temperature, the ratio of flameholder diameter to lip velocity, oxygen level, and the hydrogen-to-carbon ratio of the fuel as factors. The R-squared value of this correlation was 0.873. The exponents on the factors indicated that high pressure and temperature lowered the equivalence ratio at lean blowout, as did high levels of oxygen. The correlation for the ignition delay dataset with pressure, temperature, and the ratio of flameholder diameter to lip velocity as factors had an R-squared value of 0.942. This relatively small, uniform dataset correlates very well. When ignition delay time replaces pressure and temperature, the data continues to correlate well, with an R-squared value of 0.918. For this limited dataset, the ignition delay time is an adequate representation of the chemical timescale.</p>						
15. SUBJECT TERMS flameholder, combustor, chemical, kinetics, detonation, stabilized flame, equivalence ratio, lean blowout, R-squared						
16. SECURITY CLASSIFICATION OF:			17. LIMITATION OF ABSTRACT: SAR	18. NUMBER OF PAGES 49	19a. NAME OF RESPONSIBLE PERSON (Monitor) Andrew W. Caswell	
a. REPORT Unclassified	b. ABSTRACT Unclassified	c. THIS PAGE Unclassified			19b. TELEPHONE NUMBER (Include Area Code) N/A	

TABLE OF CONTENTS

Section	Page
List of Figures	ii
List of Tables	ii
1 Fiscal Year 2015 Technical Achievements	1
1.1 Research Objectives	1
1.2 Background of Research	1
2 Research Review	3
2.1 Studies on the Effects of Centrifugal Force on the Performance of a High-G Ultra Compact Combustor	3
2.1.1 Introduction	3
2.1.2 Gas-Phase Numerical Model	6
2.1.3 Flamelet Chemistry	7
2.1.4 Un-Normalized Progress Variable, Y_C	8
2.1.5 Turbulence-Chemistry Interaction	8
2.1.6 Thermal and Transport Properties	9
2.1.7 Boundary Conditions	10
2.1.8 Configuration Matrix	12
2.1.9 Results and Discussion	13
2.1.10 Conclusions	23
2.1.11 References	24
2.2 Influence of Fuel Characteristics on the Prediction of Lean Blowout in Bluff-body Stabilized Flames	25
2.2.1 Introduction	25
2.2.2 Experimental Setup	28
2.2.3 Correlation Results	32
2.2.4 Discussion	40
2.2.5 Conclusions	42
2.2.6 References	43

LIST OF FIGURES

Figure	Page
Figure 1. Computational Domain and Boundary Conditions.....	11
Figure 2. FLA Drawing of the Cavity Volume	12
Figure 3. FLA View of Non-reacting Flow Streamlines.....	14
Figure 4. Axial Area-averaged g-load Profiles for Various Non-reacting Configurations	15
Figure 5. FLA View of Reacting Flow Streamlines	16
Figure 6. Side View of Reacting Flow Streamlines.....	17
Figure 7. Isometric View of Temperature Contours at the Centerplane and the Periodic Boundary Condition.....	18
Figure 8. Axial Area-averaged Temperature and ϕ Profiles as a Function of Dimensionless Axial Position, L^*	19
Figure 9. Side View of the Stoichiometric Iso-surface.....	20
Figure 10. Area-averaged Axial g-loads Profiles as a Function of Dimensionless Axial Position, L^*	21
Figure 11. Area-averaged Axial S_C Profiles as a Function of Dimensionless Axial Position, L^*	22
Figure 12. Area-averaged Radial Temperature (T_{ave}) Profiles just Downstream of the IGV Trailing Edge.....	22
Figure 13. DeZubay Correlation with Data from Present Work.....	26
Figure 14. Atmospheric Pressure Combustion Rig Configuration, (A) Top View; (B) Side View.....	29
Figure 15. Atmospheric Pressure Combustion Rig.....	29
Figure 16. Validation of Cse Propane Mechanism against Flame Speed Experimental Data [23].....	32
Figure 17. Correlation Results with D/U, Temperature, and Pressure as Factors ($R^2=0.852$).....	33
Figure 18. Correlation Results with Molecular Weight as Fuel Factor ($R^2=0.858$).....	34
Figure 19. Correlation Results with Hydrogen-to-Carbon Ratio as Fuel Factor ($R^2=0.861$).....	34
Figure 20. Correlation Results with H/C and Oxygen Content, ($R^2=0.873$).....	35
Figure 21. Kariuki Parameter Plotted against Equivalence Ratio at Lean Blowout	36
Figure 22. Flame Speed Dataset Correlation Results with D/U, Temperature, and Pressure as Factors ($R^2=0.802$)	36
Figure 23. Ignition Delay Dataset Correlation Results with D/U, Temperature, and Pressure as Factors ($R^2=0.942$)	38
Figure 24. Ignition Delay Dataset Correlation Results with D/U and IDT as Factors ($R^2=0.918$).....	38
Figure 25. Ignition Delay Dataset Correlation Results with D/U as the Only Factor ($R^2=0.381$).....	39
Figure 26. Correlation Results with H/C and Oxygen Content, Showing Validation Points.....	40
Figure 27. Derived Cetane Number against Equivalence Ratio at LBO ^[28]	42

LIST OF TABLES

Table	Page
Table 1. Variables, Transport Coefficients, and Source Terms Appearing in the Governing Equation.....	7
Table 2. Configuration matrix.....	13
Table 3. Correlations Considered in This Study	30
Table 4. Hydrocarbon Structures and Their Relative Cetane Numbers and H/C Ratios	41

1 FISCAL YEAR 2015 TECHNICAL ACHIEVEMENTS

1.1 Research Objectives

Research objectives for this fiscal year include:

- Quantify and develop scaling rules for mass transport and heat release distribution in ultra-compact combustors
- Characterization of physical and chemical processes controlling stability of high-g combustors
- Assess limitations of scaling high-g combustors to larger sizes
- Quantify distribution and interaction of fuel droplets in high centrifugal force environments
- Flame distribution and heat flux interrogation during reacting film cooling
- Continue experimental and computational investigations of fundamental combustion phenomena.
- Explore the details of turbulent mixing and turbulence-chemistry interactions through studies of fundamental turbulent events.
- Investigate the physics and chemistry of combustion processes responsible for the formation of particulates.
- Characterize combustion ignition phenomena and development of novel ignition schemes.
- Develop, demonstrate, and apply advanced laser-based and other optical diagnostic techniques for the experimental characterization of key combustion phenomena.
- Develop, demonstrate, and apply advanced modeling and simulation (M&S) techniques for the computational characterization of key combustion phenomena.
- Continue efforts to integrate increasingly sophisticated chemistry and kinetics models with fluid dynamics to achieve superior combustion codes.
- Achieve a validated predictive model of turbulent mixing and turbulence-chemistry interactions.

1.2 Background of Research

During the past fiscal year, researchers with the Air Force Research Laboratory's Combustion Branch made substantial progress in numerous areas including: 1) ultra-compact combustors, 2) inter-turbine burner concepts, 3) bluff-body stabilized turbulent flames, 4) well-stirred reactors for chemical kinetics, and 5) detonation-stabilized turbulent flames.

The approaches used to meet the objectives of this program are as follows. First, experiments are performed in state-of-the-art atmospheric and high pressure/temperature facilities. A suite of diagnostics including pressure and temperature measurements, gas sampling and analysis, visual imaging, and optical (laser) measurements, are used to understand flame phenomenon and characterize the performance of combustion systems. Fundamental flame studies provide insights into fluid mechanic and chemistry effects within combustors. Larger scale experiments are used to validate combustor components and to bridge results from the fundamental flame studies to engine conditions. The second approach for meeting the research objectives is to perform modeling and simulations in conjunction with the experiments. The calculations provide further insights into combustion phenomenon and explore concepts which are not viable experimentally. Computational work includes two-dimensional calculations with full combustion chemistry and

three-dimensional simulations which capture fluid mechanic effects. Parametric studies are used to explore new design space and improve experiments. The third aspect of meeting the research objectives is using SBIR programs to support developing new technologies and transitioning this work to the warfighter. In-house testing of SBIR products supports validation of innovative concepts and leverages the high and low pressure testing capabilities within the turbine engine division.

The "Highly Loaded, Low Emissions Combustion Systems" program encompasses a range of projects from more fundamental to applied tests. The combined approach of the UCC efforts and span of research allows a pathway for aerodynamic integration of compression, combustion, and turbine airflows. This combination integrates the compressor exit guide vane along with the first stage turbine nozzle with a more compact combustor. The combination reduces airflow losses by decreasing flow angular momentum changes, resulting in a reduced pressure drop and greater engine performance in a decreased volume. These compact combustors also enable their use between the high pressure and low pressure turbines, resulting in a revolutionary, reheat cycle propulsion system called the ITB. The UCC has the potential for a 2.4 percent decrease in engine weight, 0.8% reduction in thrust specific fuel consumption, and, with an ITB, a 4,500 hp potential for additional power extraction at cruise in comparison to a Gen V fighter engine. This approach can revolutionize engine design concepts for Gen VI fighter engines.

The AFRL team was the first in the world to accomplish several groundbreaking milestones towards achieving a practical UCC. Multiple tests of a UCC were performed at engine relevant conditions. The technology demonstrated that a single cavity can be used for the combustor while maintaining appropriate heat release and temperature profiles for engines. This advancement will reduce the number of components needed for a combustor, thus decreasing the cost and complexity of the system. Evaluation of key fluid mechanic interactions between the turbine components and the combustor were performed and used to improve design rules for the system level approach.

The team developed a series of novel design and analysis tools to enable development and facilitate transitioning technology to OEMs. They designed and implemented a data processing technique to quantify visible observations from high-speed videos and provide correlations with measured combustor performance. Further, the team acquired planar laser-induced fluorescence (PLIF) measurements in the combustor; some of only a few sets of PLIF measurements collected at engine relevant conditions. The PLIF technique spatially measures flame location and heat release in the combustor, enabling validation of modeling codes using data collected non-intrusively in the flame zone. Finally, they analyzed a novel approach to reducing the number of components in the compressor and improving the UCC system for the first time. Scientific insights gained regarding cooling turbine components within a combustor, fuel droplet distribution, and interaction of flames in unconventional system will reduce the cost associated with developing and transitioning the UCC concept.

2 RESEARCH REVIEW

2.1 Studies on the Effects of Centrifugal Force on the Performance of a High-G Ultra Compact Combustor

2.1.1 Introduction

There is a need to develop advanced combustors for aircraft gas turbine engines with improved thrust-to-weight ratio, reduced gaseous emissions, and lower pressure losses and specific fuel consumption. Such combustors must preserve low maintenance cost and high durability. In order to accomplish this goal it is necessary to reduce the size of the combustors. Every inch of a combustor length reduction translates to significant weight savings (this is highly dependent on the engine size and type) [1]. Reductions in engine length and weight favorably impact engine thrust to weight ratio and fuel burn performance. A combustor with shorter length and smaller volume equates to a shorter residence time compared to conventional combustors. Since gaseous emissions such as NO_x tend to form in long residence time regions at elevated temperature, this is an advantage because these emissions would have less time to form within the combustor. However, a shorter combustor imposes some difficult challenges to overcome. A shorter, more compact combustor means that there is less time for the fuel to mix with combustor air and completely burn within the combustor. Therefore, faster mixing of fuel with air and reactants with products as well as increased turbulent flame speeds must occur. This phenomenon could potentially lead to an increase in pressure losses in order to enhance mixing.

The UCC concept combines the primary and the dilution zones of a conventional combustor with high pressure turbine inlet guide vanes (IGVs) to shorten the length of the combustor compared to a conventional design with separate combustor and IGV components. There are two general concepts of the UCC, viz., high-g cavity (HGC) and trapped-vortex cavity (TVC). Both concepts incorporate a circumferential cavity that is recessed from the mainstream flow. Liquid fuel spray and hot air are injected in this circumferential cavity (CC) where fuel evaporates and burns in a fuel-rich primary zone. Low pressure wakes transport the products, unburned fuel and intermediate species from the cavity to the mainstream flow to complete burning in a secondary zone at fuel-lean equivalence ratios. The reacted mixture then flows through the IGVs, which act as a nozzle to increase the Mach number and swirl angle for entry into the high pressure turbine rotor stage for power extraction. The HGC and TVC differ primarily in the manner in which fuel and air are injected in the recessed cavity [1,2]. For the UCC-TVC concept, air is axially injected into the cavity in non-aligned opposite directions, leading to a cavity-stabilized flame vortex with its axis tangentially aligned to the circumference of the combustor. Therefore, there is no actively forced bulk circumferential swirl flow in this concept. On the other hand, the UCC-HGC cavity air is injected inwards along the outer wall of the recessed cavity at an angle to the tangent of the cavity outer wall surface, leading to a bulk circumferential flow within the cavity around the combustor annulus. This bulk swirl in the cavity generates a high centrifugal force that acts as a buoyant-like force. It impulses the hot, lower-density reacted gases in the recessed cavity radially inwards, while pushing the colder, higher-density non-reacted gases radially outward. This allows for a shorter flame that oxidizes fuel at a “bubble” flame speed [1–3] faster than its corresponding fuel-air turbulent flame speed.

The concept of the HGC was conceived from the experiments of Lewis in the 1970's. Lewis and coworkers [4–6] used a cylindrical tube that was filled with a premixed mixture of fuel and air. Propane and hydrogen were used in these experiments. Like a propeller, the tube was rotated about its center, and once it had reached its intended rotational speed, an igniter positioned at one end of the tube sparked a flame in the fuel-air mixture. The centrifugal force induced Rayleigh-Taylor instability by negatively stratifying the mixture density in the direction of this force. Therefore, the centrifugal force is measured in factors of the Earth's gravitational acceleration. Depending on the calculated g-load, the flame propagated towards the other end of the tube at a flame propagation velocity equal or greater than the mixture's corresponding turbulent flame speed. They claimed that at low centrifugal forces (less than 500 g's) there was no effect on the propane-air flame propagation velocity. However, when the centrifugal force was increased substantially above 500 g, they claimed that the turbulent flame speed increased by up to a factor of four. They reasoned that the flame propagated at a "bubble" velocity that exceeded its corresponding turbulent flame speed. The sensitivity of the flame speed of hydrogen to g-loads was impacted by the equivalence ratio of the mixture. The flame speed of stoichiometric hydrogen-air was independent of g-load whereas that of leaner premixed hydrogen-air showed sensitivity to g-load similar to stoichiometric propane-air premixed flames. It was stated that at very high centrifugal forces of nearly 3500g the "bubble" velocity peaked and then began to decrease abruptly until the flame extinguished due to very high stretch rates.

Nonetheless, recent numerical simulations have not corroborated the effect of centrifugal force on turbulence flame speed. It is vital to point out that for a dynamic system the flame propagation velocity is not equal to the turbulent flame speed. Flame propagation velocity is the observed flame velocity from a reference frame and, hence, it is the summation of the local flow velocity and the turbulent flame speed. Katta and coworkers [1] have previously investigated this problem. They simulated Lewis' experiments by imposing a body force in the momentum equation parallel to the flow mainstream motion. However, their simulations also differ from those from Lewis and coworkers [4–6] because the tube was opened at one end. This did not allow for pressure rise that actually occurred in the experiments. However, the flame propagation characteristics compared well with Lewis experiments. Recently, Briones et al. [2] numerically examined the effect of centrifugal force on flame propagation velocity in a rotating tube that more closely mimics Lewis and coworkers experiments [4–6]. Even though there was relatively good comparison between measured [4–6] and predicted flame propagation velocity as function of centrifugal force, Rayleigh-Taylor instability with thermal expansion and turbulent flame speed constitute (in descending order) the flame propagation mechanism. In addition, Katta and coworkers [1] conducted a two-dimensional simulation where they imposed high-g forces in a JP-8 fuel-rich recessed cavity for a UCC application. They found that the high-g forces had nearly negligible effect on their two-dimensional numerical results.

Therefore, it appears that the main reason for developing a UCC-HGC with expected shorter flame that allows for a smaller combustor such as that previously investigated [1–3] is not fundamentally founded (i.e., the centrifugal force may have no effect on the turbulent flame speed). Moreover, the UCC-HGC was also conceptualized on the implicit premise that faster turbulent flame speed would translate to shorter flames. This premise also appears to be erroneous because turbulent flames are composed of multiple premixed and nonpremixed combustion regimes. The former is sensitive to turbulent flame speed whereas the latter is not. Even though turbulent flame speeds are important for flame stabilization and liftoff there is no

indication that turbulent flame speeds are relevant for flame length. For instance, Zelina and coworkers [9–11] have claimed that the UCC-HGC can achieve flame length reductions in the order of 50-70% when compared to conventional combustors. Nevertheless, it is not possible from Refs. [9–11] to discern how that conclusion was reached since turbulent flame length measurements are not discussed. Despite these controversies the UCC-HGC is still of interest because Zelina and coworkers [9–11] have demonstrated that the UCC-HGC could attain higher combustion efficiencies for a wider range of loading parameter, higher heat release rate and larger static stability than conventional combustors, while maintaining reasonable NO_x emissions.

In order to further reach a consensus on the effect of the centrifugal force on the performance of the UCC-HGC, we numerically investigate the effect of centrifugal forces on the turbulent flame speed and flame length using the UCC-HGC. For this, however, the previous UCC-HGC rig [9–11] is modified in order to operate at more realistic conditions than it did before. Zelina and coworkers operated the UCC-HGC rig [9–11] at fairly low operating pressures (~ 4 atm), low inlet temperatures (~ 550 K), low Mach numbers (~ 0.1 - 0.2) and high centrifugal forces (~ 3000 g's) mainly because the rig was not cooled and was smaller than a practical combustor. In the current investigation we have scaled and air-cooled the UCC-HGC rig so that it actually corresponds to a combustor of a relevant gas turbine engine cycle. Now, the UCC-HGC rig can operate at higher pressures (~ 19 atm), higher inlet temperature (~ 800 K) and higher Mach number (~ 0.5). The drawback is that this more practical UCC-HGC would operate at lower nominal centrifugal forces up to approximately 1700 g's. In the current investigation, nonetheless, the centrifugal force will be varied by changing the circumferential cavity (CC) air driver jets angle and pressure drop (i.e., mass flow rate or cavity loading), across the driver holes.

The purpose of this investigation is to provide further insights on whether or not centrifugal forces enhance the combustion performance of the UCC-HGC. Therefore, steady three-dimensional numerical simulations of this advanced combustor concept are performed following a multiphase, Reynolds-averaged Navier-Stokes (RANS), and flamelet/progress variable (FPV) approach using FLUENT. The specific objectives of this investigation are (1) to examine the non-reacting flow field in terms of streamlines and g-loads, (2) to inspect the reacting flow field in terms of streamlines, temperature, g-loads, and equivalence ratio (ϕ), (3) to determine the effect of averaged centrifugal force on flame length and g-loads, (4) to indirectly examine the effect of centrifugal force on the turbulent flame speed, and (5) to quantify the effect of centrifugal force on exit temperature profiles. Although there are many more quantities of interests not all can be addressed in this research.

Physical-Numerical Procedure

The commercial code FLUENT [1] has been utilized and has been customized for the simulations presented here. The fuel is injected as a liquid spray through an injector and discrete phase is used to model the transition of liquid fuel spray into gas-phase employing both Eulerian and Lagrangian frames of reference. Details of the non-adiabatic, non-premixed FPV model are presented here such as gas-phase formulation, in-house effusion cooling sources, geometries and boundary conditions.

2.1.2 Gas-Phase Numerical Model

The steady three-dimensional governing equations of continuity, momentum, turbulence, total enthalpy, mixture fraction, mixture fraction variance, and un-normalized reaction progress variable are solved using the coupled pressure-based solver of FLUENT [12]. Turbulence is modeled using the Realizable k- ϵ RANS governing equations. Turbulent kinetic energy is only generated due to mean velocity gradients. Scalable-wall functions [1,12] are used to determine the near wall flow velocity. The un-normalized progress variable variance is obtained through an algebraic equation [12]. The governing equations are discretized using second-order upwind scheme [1]. The gradients and derivatives of the governing equations are computed using the Least-Square Cell-Based Gradient [1], which is second-order spatially accurate. The discrete phase was set to interact with the continuous phase every 20 iterations. The continuity, momentum, total enthalpy, and the mixture fraction equations contain source terms that couple the continuum phase with the discrete phase. The Eulerian governing equations in differential notation can be represented in general form as follows,

$$\frac{\partial(\bar{\rho}\bar{u}\Phi)}{\partial x} + \frac{\partial(\bar{\rho}\bar{v}\Phi)}{\partial y} + \frac{\partial(\bar{\rho}\bar{w}\Phi)}{\partial z} = \frac{\partial}{\partial x}\left(\Gamma^\Phi \frac{\partial\Phi}{\partial x}\right) + \frac{\partial}{\partial y}\left(\Gamma^\Phi \frac{\partial\Phi}{\partial y}\right) + \frac{\partial}{\partial z}\left(\Gamma^\Phi \frac{\partial\Phi}{\partial z}\right) + S^\Phi \quad (1)$$

Depending on the value of Φ , this equation represents the continuity, momentum, turbulent kinetic energy, eddy dissipation rate, total enthalpy, mixture fraction, mixture fraction variance, and un-normalized reaction progress variable equations, as shown in Table 1. This table also describes the transport coefficient Γ^Φ and the source term S_Φ for each equation. Further details regarding the model constants, and β -shape PDF can be found in Refs. [1–3]. Source and sink terms in the continuity and enthalpy equations are used to model effusion cooling. These are indicated by the first term in the S_Φ column of Table 1.

Discrete Phase Model

Note that the second terms in the S_Φ column, the last terms in the momentum equations and the only term in the mixture fraction equations are the sources for the DPM interaction with the Eulerian phase. Briefly, the fuel liquid droplet trajectory is calculated by integrating the force balance on the droplet by equating the particle inertia with the drag force and considering turbulent dispersion. The droplets evaporate when the droplet temperature (T_p) is higher than the saturation temperature (T_{sat}) and lower than the boiling point (T_{BP}) of JP8. Under evaporation the JP8 liquid particle receives heat from the continuum phase while transferring mass to the gaseous phase. For more details refer to Refs. [3, 16, 17].

Table 1. Variables, Transport Coefficients, and Source Terms Appearing in the Governing Equation

Equations	Φ	Γ_Φ	S_Φ
Continuity	1	0	$\frac{\dot{m}_b}{V_{\text{cell}}} + \frac{\dot{m}_{p,\text{in}} - \dot{m}_{p,\text{out}}}{\dot{m}_{p,0} V_{\text{cell}}} \dot{m}_{p,0}$
Spanwise Momentum	\tilde{u}	$\mu + \mu_t$	$-\frac{\partial \bar{p}}{\partial x} + \frac{\partial}{\partial x} \left((\mu + \mu_t) \frac{\partial \tilde{u}}{\partial x} \right) + \frac{\partial}{\partial y} \left((\mu + \mu_t) \frac{\partial \tilde{v}}{\partial x} \right) + \frac{\partial}{\partial z} \left((\mu + \mu_t) \frac{\partial \tilde{w}}{\partial x} \right) - \frac{\partial \tau_{xx}^{\text{turb}}}{\partial x} - \frac{\partial \tau_{xy}^{\text{turb}}}{\partial y} - \frac{\partial \tau_{xz}^{\text{turb}}}{\partial z} + \sum \left[\frac{18\mu}{\rho_p d_p^2} \frac{C_D \text{Re}_p}{24} \left(u_p - \left(\tilde{u} + \xi \sqrt{\frac{2k}{3}} \right) \right) \right] \frac{\dot{m}_p \Delta t}{V_{\text{cell}}}$
Transverse Momentum	\tilde{v}	$\mu + \mu_t$	$-\frac{\partial \bar{p}}{\partial y} + \frac{\partial}{\partial x} \left((\mu + \mu_t) \frac{\partial \tilde{u}}{\partial y} \right) + \frac{\partial}{\partial y} \left((\mu + \mu_t) \frac{\partial \tilde{v}}{\partial y} \right) + \frac{\partial}{\partial z} \left((\mu + \mu_t) \frac{\partial \tilde{w}}{\partial y} \right) - \frac{\partial \tau_{yx}^{\text{turb}}}{\partial x} - \frac{\partial \tau_{yy}^{\text{turb}}}{\partial y} - \frac{\partial \tau_{yz}^{\text{turb}}}{\partial z} + \sum \left[\frac{18\mu}{\rho_p d_p^2} \frac{C_D \text{Re}_p}{24} \left(v_p - \left(\tilde{v} + \xi \sqrt{\frac{2k}{3}} \right) \right) \right] \frac{\dot{m}_p \Delta t}{V_{\text{cell}}}$
Streamwise Momentum	\tilde{w}	$\mu + \mu_t$	$-\frac{\partial \bar{p}}{\partial z} + \frac{\partial}{\partial x} \left((\mu + \mu_t) \frac{\partial \tilde{u}}{\partial z} \right) + \frac{\partial}{\partial y} \left((\mu + \mu_t) \frac{\partial \tilde{v}}{\partial z} \right) + \frac{\partial}{\partial z} \left((\mu + \mu_t) \frac{\partial \tilde{w}}{\partial z} \right) - \frac{\partial \tau_{zx}^{\text{turb}}}{\partial x} - \frac{\partial \tau_{zy}^{\text{turb}}}{\partial y} - \frac{\partial \tau_{zz}^{\text{turb}}}{\partial z} + \sum \left[\frac{18\mu}{\rho_p d_p^2} \frac{C_D \text{Re}_p}{24} \left(w_p - \left(\tilde{w} + \xi \sqrt{\frac{2k}{3}} \right) \right) \right] \frac{\dot{m}_p \Delta t}{V_{\text{cell}}}$
Turbulent Kinetic Energy	k	$\mu + \frac{\mu_t}{\sigma_k}$	$\underbrace{\mu_t \left[\left(\frac{\partial \tilde{u}}{\partial x} \right)^2 + \left(\frac{\partial \tilde{v}}{\partial y} \right)^2 + \left(\frac{\partial \tilde{w}}{\partial z} \right)^2 + \frac{1}{2} \left(\frac{\partial \tilde{u}}{\partial y} + \frac{\partial \tilde{v}}{\partial x} \right)^2 + \frac{1}{2} \left(\frac{\partial \tilde{w}}{\partial y} + \frac{\partial \tilde{v}}{\partial z} \right)^2 + \frac{1}{2} \left(\frac{\partial \tilde{u}}{\partial z} + \frac{\partial \tilde{w}}{\partial x} \right)^2 \right]}_{SR^2} - \rho \varepsilon$
Eddy Dissipation Rate	ε	$\mu + \frac{\mu_t}{\sigma_\varepsilon}$	$\rho \cdot \max \left(0.43, \frac{SR \cdot k / \varepsilon}{5 + SR \cdot k / \varepsilon} \right) \cdot \left[\left(\frac{\partial \tilde{u}}{\partial x} \right)^2 + \left(\frac{\partial \tilde{v}}{\partial y} \right)^2 + \left(\frac{\partial \tilde{w}}{\partial z} \right)^2 + \frac{1}{2} \left(\frac{\partial \tilde{u}}{\partial y} + \frac{\partial \tilde{v}}{\partial x} \right)^2 + \frac{1}{2} \left(\frac{\partial \tilde{w}}{\partial y} + \frac{\partial \tilde{v}}{\partial z} \right)^2 + \frac{1}{2} \left(\frac{\partial \tilde{u}}{\partial z} + \frac{\partial \tilde{w}}{\partial x} \right)^2 \right] + \frac{1}{2} \left(\frac{\partial \tilde{u}}{\partial z} + \frac{\partial \tilde{w}}{\partial x} \right)^2 \right]^{1/2} \varepsilon - 1.9 \rho \frac{\varepsilon^2}{k + \sqrt{\mu_t \varepsilon / \rho}}$
Mean Total Enthalpy	\tilde{H}	$\lambda + \frac{\mu_t}{Pr_t}$	$\frac{\dot{m}_b}{V_{\text{cell}}} \int_{T_{\text{ref}}}^{T_{p,\text{out}}} c_{p,\text{air}} d\tilde{T} + \frac{\dot{m}_{p,0}}{\dot{m}_{p,0} V_{\text{cell}}} \left[(\dot{m}_{p,\text{out}} - \dot{m}_{p,\text{in}}) h_{fg} - \dot{m}_{p,\text{out}} \int_{T_{\text{ref}}}^{T_{p,\text{out}}} c_{p,p} d\tilde{T} + \dot{m}_{p,\text{in}} \int_{T_{\text{ref}}}^{T_{p,\text{in}}} c_{p,p} d\tilde{T} \right]$
Mean Mixture Fraction	\tilde{f}	$\frac{\mu_t}{\sigma_f}$	$\frac{\dot{m}_{p,\text{out}} - \dot{m}_{p,\text{in}}}{\dot{m}_{p,0} V_{\text{cell}}} \dot{m}_{p,0}$
Mean Mixture Fraction Variance	$\widetilde{f^2}$	$\frac{\mu_t}{\sigma_f}$	$2.86 \cdot \mu_t \left(\frac{\partial \tilde{f}}{\partial x} + \frac{\partial \tilde{f}}{\partial y} + \frac{\partial \tilde{f}}{\partial z} \right)^2 - 2.0 \cdot \rho \frac{\varepsilon}{k} \widetilde{f^2}$
Progress Variable	$\widetilde{Y_c}$	$\frac{\mu_t}{Sc_t}$	S_C

2.1.3 Flamelet Chemistry

N-dodecane is used as a single surrogate component for JP8. The flamelets were calculated by solving the laminar n-C₁₂H₂₆/air counterflow non-premixed flame equations in a mixture fraction space [1, 2] using the JetSurf-1.0 [1] chemical reaction mechanism containing 194 species and 1459 Arrhenius reactions. Several flamelets for various scalar dissipation, χ , rates were computed.

2.1.4 Un-Normalized Progress Variable, Y_C

The dimensionless C-progress variable previously used [1–3] is replaced by the un-normalized reaction progress variable, Y_C . The relationship between the C-progress variable and the Y_C is as follows.

$$C = \frac{Y_{co} + Y_{co_2}}{Y_{co}^{eq}(\tilde{f}) + Y_{co_2}^{eq}(\tilde{f})} = \frac{Y_c}{Y_c^{eq}} \quad (2)$$

Y_C is defined as the summation of the CO and CO₂ mass fractions. Note that this definition is not unique and could have also been defined in many other ways. The C progress variable is the ratio of local Y_C and the local equilibrium Y_C . It is more advantageous to solve for Y_C than for C. This is because the latter requires modeling of the source terms based on the laminar flame speed and Zimont model. On the contrary, the former transport equation can achieve closure of the source terms by recalling the CO and CO₂ net reaction rates from the FGM. This, in turn, provides another benefit. That is, the source term in Y_C is not just now dependent on C but also on f. This implies that when $\tilde{C} = 1$, additional air dilution can actually quench the flame (i.e., \tilde{Y}_C will be reduced and \tilde{C} will fall below unity).

2.1.5 Turbulence-Chemistry Interaction

The turbulence-chemistry interaction is modeled using probability density functions (PDFs), which can be thought as the amount of time a fluid particle spends in the vicinity of a state, determined by mixture fraction (f), progress variable (c), and total enthalpy (H). The FGM's variable Φ takes the values of ρ , Y_i , T, and S_{FR} . The triple integral of the product of Φ and its PDFs gives the averaged value of $\tilde{\Phi}$ in the three-dimensional spatial domain. This general equation is presented below.

$$\tilde{\Phi} = \int_{H_{loss}}^{H_{gain}} \int_0^1 \int_0^1 \Phi(f, c, H) \text{PDF}(f, c, H) df dc dH \quad (3)$$

Note that f and c are integrated from 0 to 1, whereas H is integrated from the user's input of H_{gain} to H_{loss} . The latter is needed for non-adiabatic cases like the current model. By decomposing the PDF into three independent PDFs the following equation is obtained.

$$\tilde{\Phi} = \int_{H_{loss}}^{H_{gain}} \int_0^1 \int_0^1 \Phi(f, c, H) \text{PDF}(f) \text{PDF}(c) \text{PDF}(H) df dc dH \quad (4)$$

For the mixture fraction (f) and progress variable (c), β presumed PDFs are used. These requires second moments (i.e., variances) for f and c. The mixture fraction variance (\tilde{f}^2) is obtained by a solving transport equation as shown in Table 1. The c-progress variable variance is obtained from the following algebraic consideration.

$$\tilde{c}^2 = \frac{\tilde{Y}_c^2}{(Y_c^{eq})^2} = \frac{0.1 \frac{l_t^2}{Sc_t} (\nabla \tilde{Y}_c)^2}{\left(Y_{co}^{eq}(\tilde{f}) + Y_{co_2}^{eq}(\tilde{f})\right)^2} \quad (5)$$

For the PDF(H), a δ presumed probability function is used. This turns the above equation into the following.

$$\tilde{\Phi} = \int_0^1 \int_0^1 \Phi(f, c, H) \beta(f) \beta(c) \delta(\tilde{H} - H) df dc \quad (6)$$

Now the thermochemical table can be constructed for the variables $\tilde{\Phi} = \tilde{\rho}$, \tilde{Y}_i , \tilde{T} , and \tilde{S}_{FR} as function of f , c and H . The multiple flamelets scalar dissipation rates, χ , are dropped out by calculating c along a flame. Note below that \tilde{Y}_i is a function of only f and c within the flame region ($0 < c < 1$) in order to reduce the number of flamelets computed. However, \tilde{Y}_i is also a function of H at equilibrium conditions ($c = 1$).

$$\tilde{\rho} = \int_0^1 \int_0^1 \rho(f, c, H) \beta(f) \beta(c) \delta(\tilde{H} - H) df dc \quad (7)$$

$$\tilde{Y}_i = \int_0^1 \int_0^1 Y_i(f, c) \beta(f) \beta(c) df dc, 0 < c < 1 \quad (8)$$

$$\tilde{Y}_i = \int_0^1 \int_0^1 Y_i(f, H) \beta(f) \delta(\tilde{H} - H) df dc, c = 1 \quad (9)$$

$$\tilde{T} = \int_0^1 \int_0^1 T(f, c, H) \beta(f) \beta(c) \delta(\tilde{H} - H) df dc \quad (10)$$

$$\tilde{S}_{FR} = \int_0^1 \int_0^1 S_{FR}(f, c) \beta(f) \beta(c) df dc \quad (11)$$

Note that $S_{FR}(f, c)$ is just the summation of the net reaction rates of CO and CO₂ (i.e., $S_{FR} = \dot{\omega}_{CO} + \dot{\omega}_{CO_2}$). Moreover, although the transport equations solve for \tilde{Y}_c this value has to be converted to C through Eq. 2 in order to interact with the thermochemical table. When local strain rate weakens the turbulent flame in the flow field the value of C is less than unity for a given \tilde{f} . If local strain rate is excessive the C is zero and the flame quenches locally.

2.1.6 Thermal and Transport Properties

The default values for mixture molecular viscosity (μ) and thermal conductivity (λ) in FLUENT are constant. This, however, does not correspond to the reality of the current conditions. Combustion converts the reactant's enthalpy of formation into sensible enthalpy, raising the flow temperature. This, in turn, decreases the density (ρ) up to six times, while accelerating the flow velocity through the flame and increasing μ and λ . The overall effect of combustion is to locally lower the Reynolds number. Hence, the molecular transport properties become relatively important as their turbulent counterparts in the vicinity of the flame-front and high temperature regions. Therefore, we developed, debugged, compiled and linked a C-programming user-defined function (UDF) to account for the mixture temperature- and species-dependent μ and λ . The code reads the transport properties for all species involved in the flamelet generation. Then, it compares these species with those available in the PDF look-up table (i.e., 20 most abundant species stored for current results). The code automatically extracts the species molecule index, L-J potential, L-J collision diameter, polarizability and the rotational relaxation number [23]. At the beginning of each iteration, the code computes the individual species μ_i and λ_i using the standard kinetic theory [1, 2] and the kinetic theory approach given by Warnatz [22, 26], respectively. The mixture molecular transport properties needed in the equations in Table 1 are obtained from μ_i and λ_i using Wilke semi-empirical equations [22, 27]. The in-house UDF was compared with calculations performed using NASA CEA [28] and they compared remarkably well when comparing μ and λ as a function of ϕ (not shown). This comparison also revealed that if

temperature-dependent air properties were to be used alone, instead the error in λ would be up 50% at fuel-rich conditions. Furthermore, the transport kinetic theory formulation is computationally expensive, slowing down iterations about 5 times. Thereby, to mitigate this drawback we blended the transport kinetic theory with air temperature-dependent properties. At low temperatures, below 850K, the latter transport properties would be used whereas at higher temperature the former transport properties would be utilized. This only slowed down the calculations about 2.5 times. Finally, the mixture specific heat capacity (c_p) essential for calculating the temperature from the enthalpy equation is obtained from a mixing law (i.e., $c_p = \sum_i \tilde{Y}_i \cdot c_{p,i}$).

2.1.7 Boundary Conditions

Figure 1 presents the computational domain and boundary conditions. The UCC-HGC is modeled as a 60° rotational periodic sector. The geometry is represented by pressure inlet, mass flow inlet, and wall boundary conditions. The UCC-HGC is fed by a plenum associated with the mainstream flow and the CC driver jets. Therefore, this plenum is modeled as pressure inlet boundary conditions. The corner cooling jets are also modeled as pressure inlet boundary condition. The outflow is modeled with mass flow outlet boundary condition. The reason for using inlet pressure and mass outlet boundary conditions is because the various UCC-HGC configurations studied here are compared at constant mass flow rate, operating pressure, and inlet temperature, while the mass flow split between mainstream and CC driver jets is varied at constant global equivalence ratio (ϕ_{Global}). The rest of the walls are modeled as impermeable adiabatic wall boundary conditions. The operating pressure of the combustor is 1,945 kPa. The fuel is injected as liquid from a cone injector located at the centroid of the outer surface of the cavity-in-cavity (CIC) feature. The injector is normal to the CIC and CC and its half angle of injection is set to $\theta_{1/2} = 45^\circ$ with a logarithmic Rosen-Rammler droplet distribution with spread factor of 3.5 varying from 0.1 to 100 μm . The average diameter is 20 μm . The fuel droplets can escape the inlet and outlet boundaries, whereas they bounce off the walls. The boundary conditions for the continuum and discrete phase governing equations presented before are as follows:

Pressure Inlet Boundary Condition

$$\tilde{P} = 134 \text{ kPa (gauge)}, \quad \tilde{T} = 810.927 \text{ K}, \quad \tilde{Y}_c = 0, \quad \tilde{f} = \tilde{f}^{\sim 2} = 0, \quad u' = 0.05\tilde{u}, \quad l_{\text{turb}} = D_H$$

Mass Flow Outlet Boundary Condition

$$\dot{m} = 0.564 \frac{\text{kg}}{\text{s}} \text{ (per sector)}$$

Wall Boundary Condition

$$\tilde{u} = \tilde{v} = \tilde{w} = 0, \quad \nabla_n \tilde{Y}_c = \nabla_n \tilde{f} = \nabla_n \tilde{f}^{\sim 2} = \nabla_n \tilde{H} = 0, \quad k = \epsilon = 0, \quad \vec{v}_p \cdot \hat{n}_w = -\vec{v}_p \cdot \hat{n}_w, \quad \text{and} \quad \vec{v}_p \cdot \hat{t}_w = \vec{v}_p \cdot \hat{t}_w$$

Discrete Phase Injections

$$\dot{m}_p = 0.0189 \text{ kg/s (per injector)}, \quad |\vec{v}_p| = 93 \text{ m/s}, \quad T_p = 296.8 \text{ K}, \quad \theta_{1/2} = 45^\circ, \quad d_{p,\text{min}} = 0.1 \mu\text{m}, \quad d_{p,\text{avg}} = 20 \mu\text{m}, \quad d_{p,\text{max}} = 100 \mu\text{m}$$

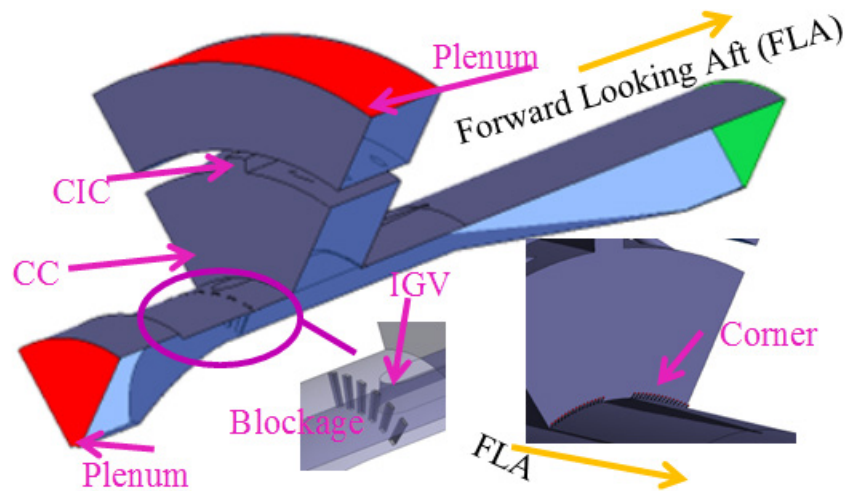


Figure 1. Computational Domain and Boundary Conditions

(The types of boundary conditions are color coded in red, representing pressure inlet boundary conditions, green, representing mass flow outlet, and gray, representing impermeable adiabatic wall boundary conditions. The orange arrows indicate the locations at which the injector is mounted onto the circumferential cavity (CC). The various components of the UCC-HGC are labeled. The labels are colored with the applied boundary condition.)

The mass and enthalpy sink terms that appear in Table 1 are applied to the lower surface of the plenum adjacent to the CC jets. Then, there are equivalent mass and enthalpy source terms adjacent to the outer CC surface as well as the outer and side surfaces of the CIC. Here the sink and source terms are balanced. These sink and source terms mimic the fluid flow from the plenum volume through the effusion cooling holes of the outer CC surface of the cavity. In addition, there are mass and enthalpy source terms applied to the forward and aft surfaces of the CC as well as to the outer liner immediately downstream the CC but ends near the trailing edge of the IGV. These mass source terms model the air effusion cooling through each of these surfaces.

Mesh

We performed global mesh sensitivity analysis because there are nine geometries to consider. Our approach was the following. We created two mesh sizes for the nine configurations reported here, viz., 2.5 and 10 million cells. Non-reacting flow simulations were performed for these mesh size and the discharge coefficient was computed for the core and CC jets. Results indicated that the discharge coefficient was nearly independent of mesh size. The discharge coefficient for the core flow and the CC jets was in the vicinity of 0.77 and 0.69, respectively. We decided to use the 10 million cell mesh to avoid any grid sensible results. The mesh is unstructured, formed by tetrahedral elements in the core and prism elements for the boundary layers. The minimum and maximum cell sizes for the tetrahedral elements are 0.50 and 1.50 mm, respectively. Ten inflation layers with initial height of 0.1 mm are used for the prismatic boundary layers. We decided to use scalable wall functions to address the shear layer near the walls. The mesh maximum stretch factor is 1.2.

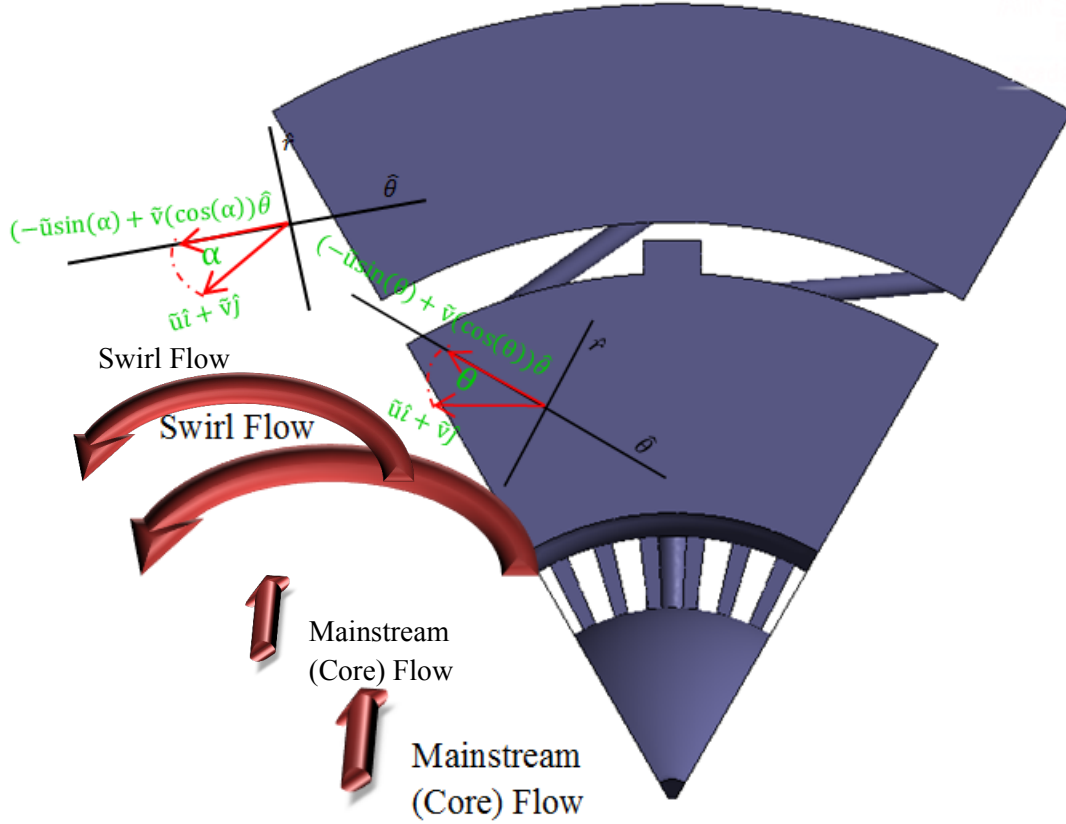


Figure 2. FLA Drawing of the Cavity Volume

(The figure shows the driver jet tangential velocity $(-\tilde{u}\sin(\alpha) + \tilde{v}(\cos(\alpha)))$ and its angle of inclination (α) as well as the general representation for calculating the flow tangential velocity $(-\tilde{u}\sin(\theta) + \tilde{v}(\cos(\theta)))$ in the domain. The Cartesian (\hat{i}, \hat{j}) and cylindrical ($\hat{r}, \hat{\theta}$) unit vector are displayed.)

2.1.8 Configuration Matrix

The steady volumetric centrifugal force on a fluid particle in the cavity flow is depicted in Figure 2 and can be summarized as:

$$F_c = \rho \cdot (g - \text{loads}) \cdot g \text{ and } g - \text{loads} = \left[\frac{(-\tilde{u}(\sin(\theta)) + \tilde{v}(\cos(\theta)))^2}{gr} \right] \quad (12)$$

Note that the numerator is just the tangential velocity everywhere in the domain defined by the Cartesian spanwise (\tilde{u}) and transverse (\tilde{v}) velocities and by the circumferential coordinate, θ . The two parameters that were chosen to vary centrifugal force were the jet flow inclination angle (α_{jet}) and the cavity mass flow rate (\dot{m}_{CC}). It is expected that the g-load should increase with decreasing α_{jet} (cf. Eq. 12) and with increasing \dot{m}_{CC} . The three chosen α_{jet} are represented in the configuration identification names as numbers and are as follows: 1 is 20.0°, 2 is 32.5°, and 3 is 45.0°. The cavity mass flow rate (\dot{m}_{CC}) is varied by changing the diameter of the driver jet holes because the pressure drop across the holes is constant for all cases. In order to maintain constant total air flow and global equivalence ratio (ϕ_{Global}), the mainstream mass flow must decrease with increasing \dot{m}_{CC} . Thus, a blockage plate with vertical slots as shown in Figure 1 is used to meter this mainstream flow. By reducing the core flow with higher metering plate

blockage, we increase the diameter cavity driver jets so that the combination of the core flow and the cavity driver jet flow is maintained nearly constant. Therefore, the resulting parameter is a CC-to-core area ratio where the core area is the open area through the blockage plate and the CC area is the total area of the driver jets. The three chosen ratios are represented in the configuration identification names as letters and are as follows: “a” is 0.22, “b” is 0.41, and “c” is 0.74. Note that increasing the CC-to-core area ratio directly increases $\dot{m}_{CC}/\dot{m}_{core}$, and increases the cavity loading while leaning out the CC. There are a total of nine configurations investigated here, and they are shown in Table 2.

Table 2. Configuration matrix

CC Jet Angle (α_{jet})	CC-to-core Area Ratio		
	0.22	0.41	0.74
20.0°	1a	1b	1c
32.5°	2a	2b	2c
45.0°	3a	3b	3c

Table Note: There are three CC jet angles (α_{jet}) and for each there are three CC-to-core area ratios for a total of nine configurations. The alphanumeric values in the table are the configuration identification names.

2.1.9 Results and Discussion

In this section we initially discuss the non-reacting flow field. Subsequently, we examine the reacting flow field for various UCC-HGCs. Then, we determine the effect of averaged centrifugal force on g-loads and flame length. Next, we inspect the effect of centrifugal force on the turbulent flame speed. Finally, we quantify the effect of averaged centrifugal force on exit temperature profiles.

Non-reacting Flow Field

The non-reacting flow field is examined in terms of streamlines and g-loads. Figure 3 and Figure 4 present the streamlines and area-averaged axial g-load profiles, respectively. Because the streamline flow structure for the various configurations under non-reacting flow conditions is qualitatively similar, Figure 3 only illustrates the flow field for configuration 1a. Note here that a plenum feeds the CC jets and some (blue) streamlines end at the CC outer surface because of the mass and enthalpy sink terms imposed here to mimic transpiration. Within the CC the flow field is very stratified with the circumferential flow marked by blue streamlines circulating tangent to the outer cavity wall. The mainstream flow (red) does not enter into the CC. The cooling jets are washed out and remain near the liner outer surface.

Figure 4 clearly illustrates that there are multiple g-load peaks that are consistent and that are independent of the configuration. The two rows of CC air driver jets produce two g-load maxima. The magnitude of the pair of g-load peaks in the CC varies chiefly as function of $\dot{m}_{CC}/\dot{m}_{core}$ and secondly as a function of jet angle (α_{jet}). As α increases, the CC g-load decreases from 1283 to 916g’s for series a, from 2661 to 1809g’s for series b, and from 4584 to 3400g’s for series c. Finally, the effect of α_{jet} becomes more pronounced at higher $\dot{m}_{CC}/\dot{m}_{core}$. The trends seen in the non-reacting flow results are consistent with the trends inferred by Eqs. 12 and Figure 2.

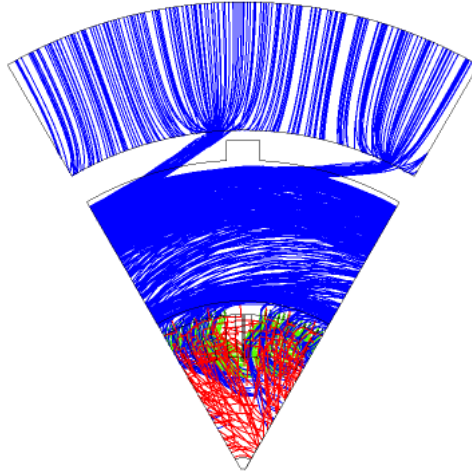


Figure 3. FLA View of Non-reacting Flow Streamlines

(The non-reacting flow streamlines are emanating from the mainstream plenum (red), the CC plenum (blue), and the cooling jets (green) for the configuration 1a discussed in the context of Table 2.)

Reacting Flow Field

Now we discuss the reacting flow field for various UCC-HGC configurations. Figure 5 and Figure 6 present, respectively, the forward looking aft (FLA) and side views of the reacting flow streamlines emanating from the mainstream plenum (red), the CC plenum (blue), and the cooling jets (green). It is clear from Figure 5 that the presence of the flame and the resulting volumetric expansion has somewhat distorted the (strong) uniform CC bulk swirl that was present under non-reacting flow conditions (cf. Figure 3 and Figure 5). However, the plenum that feeds the CC jets does not seem to be affected by combustion and streamlines still end at the CC outer wall due to the mass and enthalpy sink terms that mimic effusion cooling. All configurations exhibit nearly negligible mainstream flow entraining into the CC like their non-reacting flow counterparts (cf. Figure 3). In addition, Figure 5 shows that as $\dot{m}_{CC}/\dot{m}_{core}$ increases the cavity streamlines tend to initially stay close to the cavity outer wall surface before turning radially inward towards the core flow. This would likely contribute to higher centrifugal force, locally, along the cavity outer wall surface. The large regions in the cavity without streamlines in configurations 2b, and 2c show that large recirculation zones may exist near the CC outer wall.

The side view of the UCC-HGC configurations in Figure 6 shows details of the axial distribution of the cavity driver air. For all configurations, the swirling cavity flow tends to migrate to the downstream (aft) wall of the cavity before exiting into the mainstream. This may be due to the dynamic pressure exerted by the mainstream flow on the shear region between the two flows. As α increases from configurations 1 to 3, the driver jet air penetrates deeper into the CC.

Qualitatively, it appears that with increasing α the CC jet (blue) streamlines mixed better with the mainstream and cooling flow as illustrated by Figure 6. It appears that there is no significant trend of $\dot{m}_{CC}/\dot{m}_{core}$ on the exit streamlines.

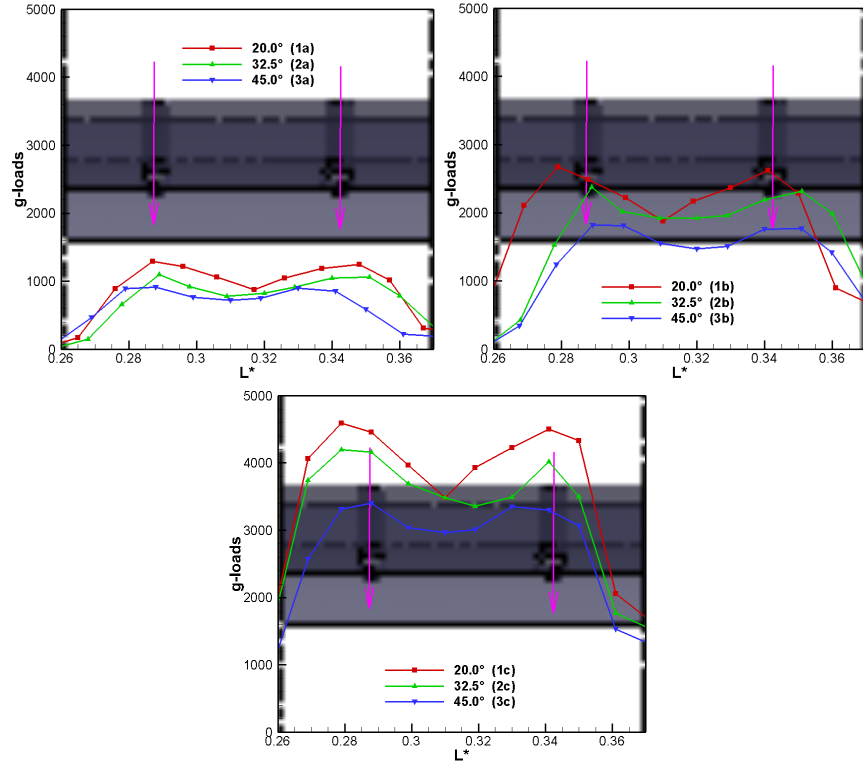


Figure 4. Axial Area-averaged g-load Profiles for Various Non-reacting Configurations
(The configurations are discussed in the context of Table 2. The region of interest is from the CC forward wall to the CC aft wall. The magenta arrows indicate the location of the CC air driver jets.)

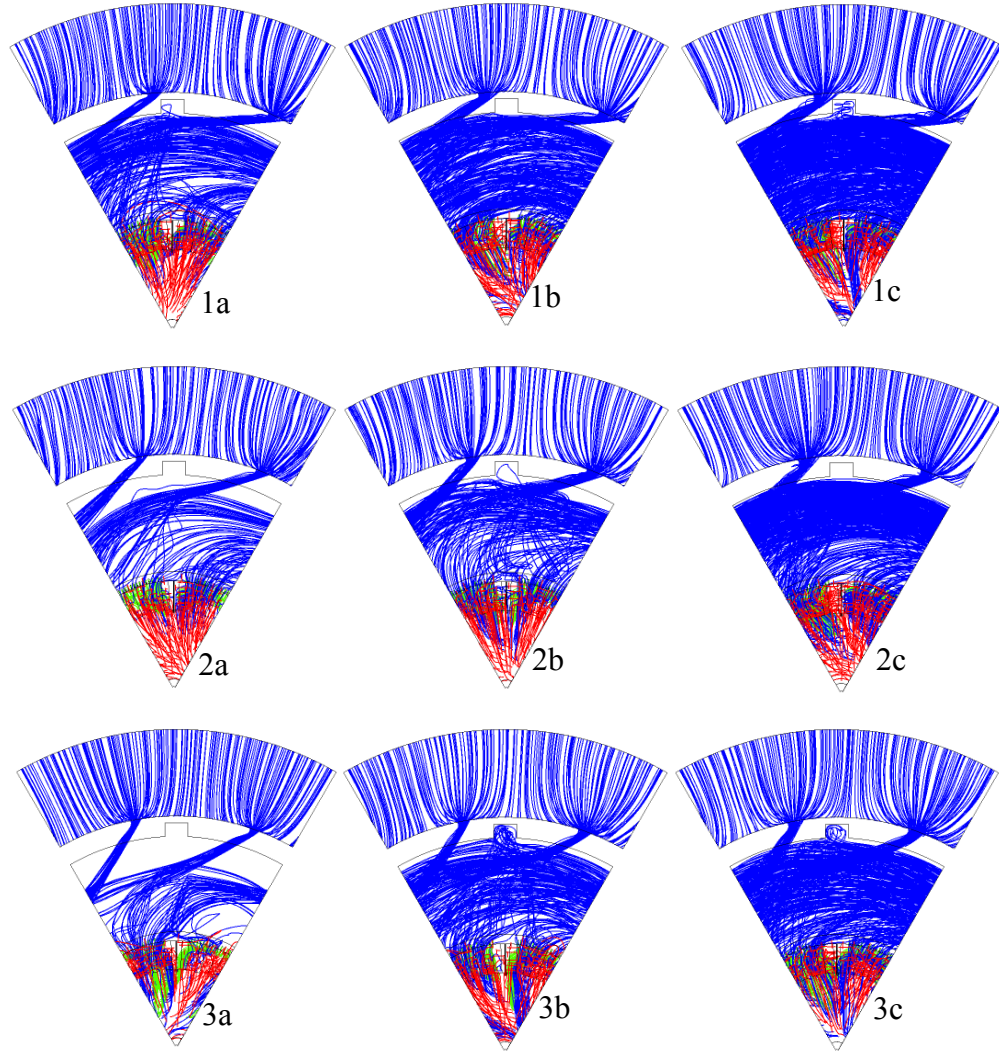


Figure 5. FLA View of Reacting Flow Streamlines

(The reacting flow streamlines emanate from the mainstream plenum (red), the CC plenum (blue), and the cooling jets (green) for the configurations discussed in Table 2.)

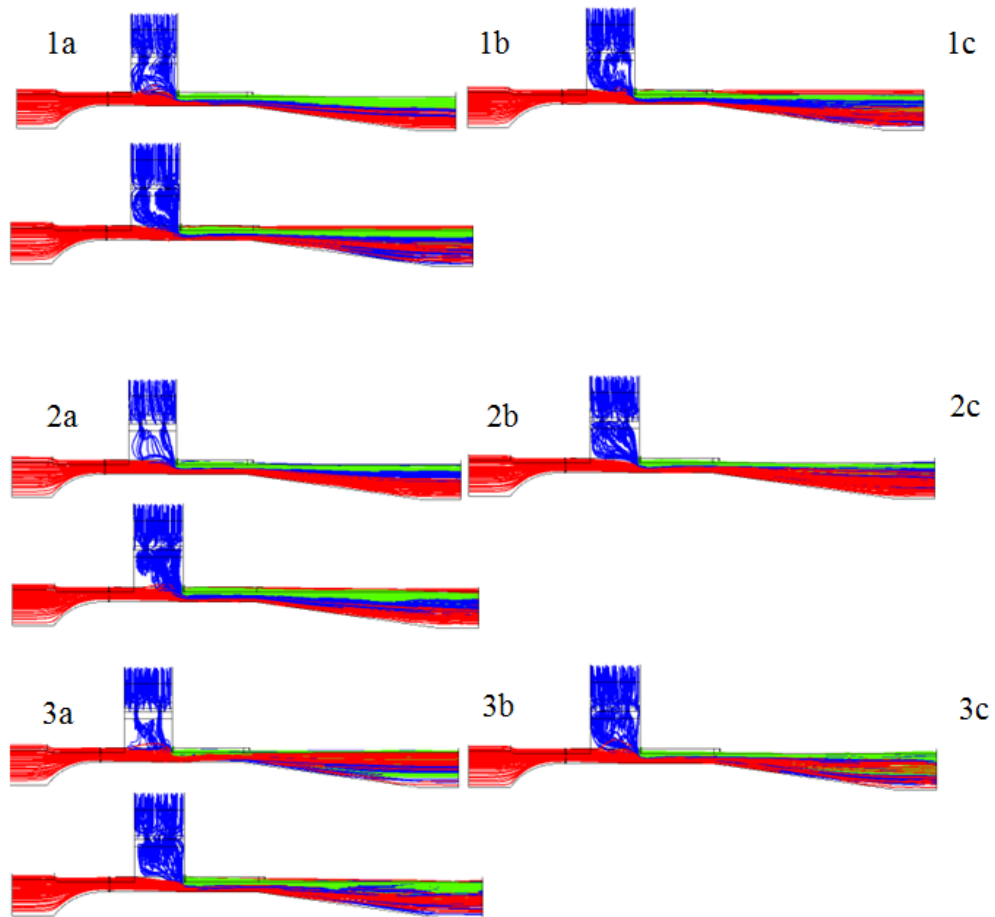


Figure 6. Side View of Reacting Flow Streamlines

(The reacting flow streamlines are emanating from the mainstream plenum (red), the CC plenum (blue), and the cooling jets (green) for the configurations discussed in the context of Figure 5.)

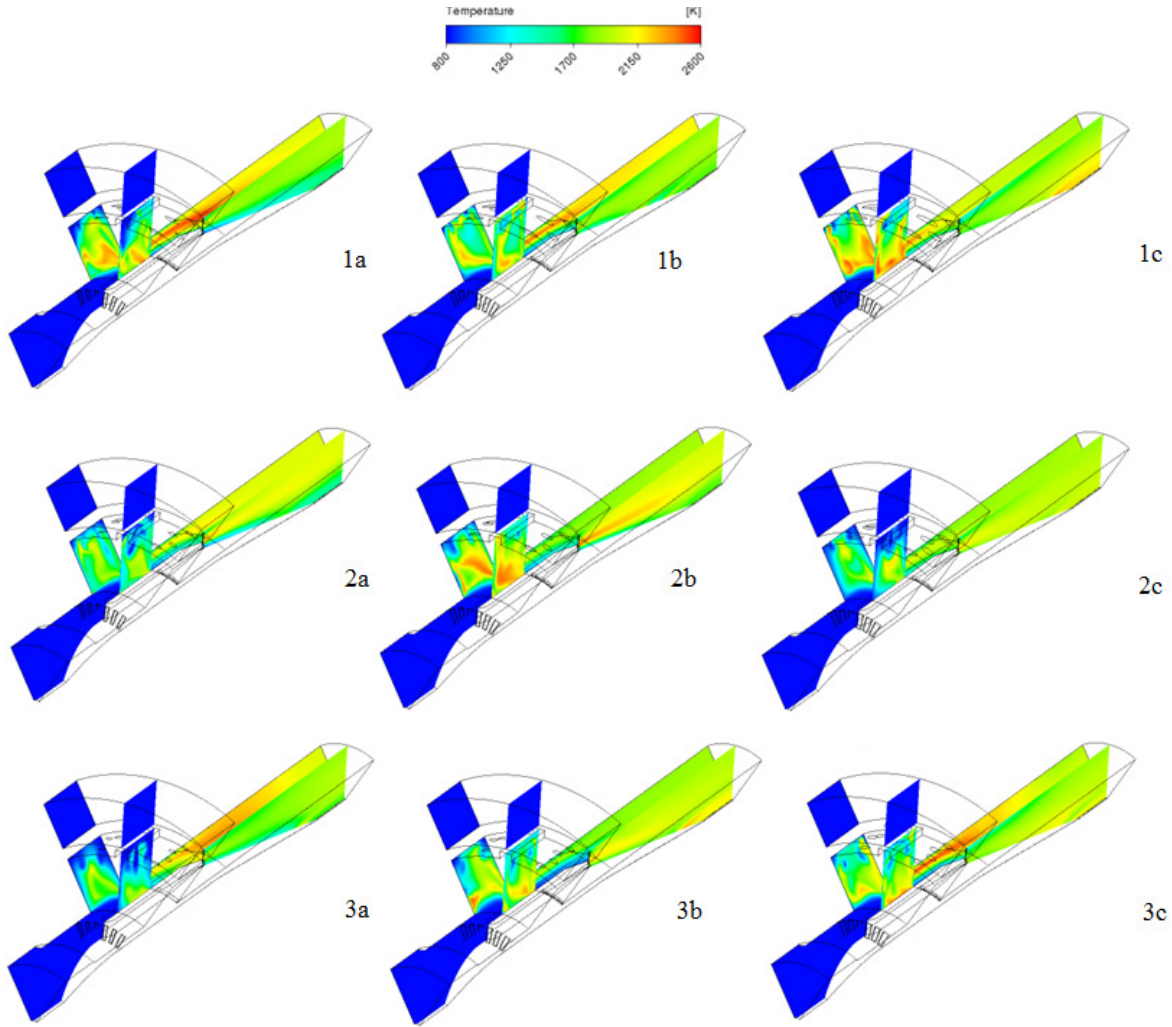


Figure 7. Isometric View of Temperature Contours at the Centerplane and the Periodic Boundary Condition

(The contour views are for the configurations discussed in the context of Figure 5. The units are in Kelvin.)

Temperature contours at two circumferential locations, viz., centerplane and periodic boundary, are illustrated in Figure 7. Plenum air enters the flow domain at the mainstream and cavity pressure inlets. Temperature rise begins within the circumferential cavity, and the temperature continues to rise downstream of the CC. The temperature in the cavity is generally highest toward the centerplane. The air-cooled walls tend to keep hot products away from the surfaces. It is evident from this figure that configurations with $\alpha_{jet}=20.0^\circ$ (1a, 1b, and 1c) have relatively higher temperatures in the CC than the other configurations. Interestingly, configurations 2b also attained relatively higher temperature region within the CC. Lastly, there is no discernable effect of $\dot{m}_{CC}/\dot{m}_{core}$ on the temperature contours.

The temperature contours presented in Figure 7 can be better analyzed by conducting data reduction. This is done by plotting the area-averaged axial temperature profiles in Figure 8. Because the local equivalence ratio, ϕ , is one of the variables that determines the flame temperature, the area-averaged ϕ as a function of dimensionless axial distance (L^*) is shown for

all configurations. These results indicate that for all the configurations the temperature in the CC is lower (1300-1800K) than the end of the rig (ca. 2000K). Importantly, the temperature does not reach its maximum temperature by the trailing edge of the vane; indeed, it continues increasing slightly through the expansion region over the centerbody. This indicates further burning is occurring in this expansion region. The implication of this result is that a UCC-HGC would actually end at the IGV trailing edge and further burning would continue towards the turbine. This result would be detrimental for proper engine operation. The relatively lower area-averaged temperature region inside the CC is partly due to the higher ϕ , well above stoichiometry. For all configurations the temperature at the exit of the rig is ca. 2000 K because the $\phi_{\text{Global}}=0.53$ for all configurations, as indicated at $L^*=1$. This is consistent with equilibrium gas temperature calculations for Jet-A type fuel at the rig operating pressure, inlet air temperature, and ϕ_{Global} .

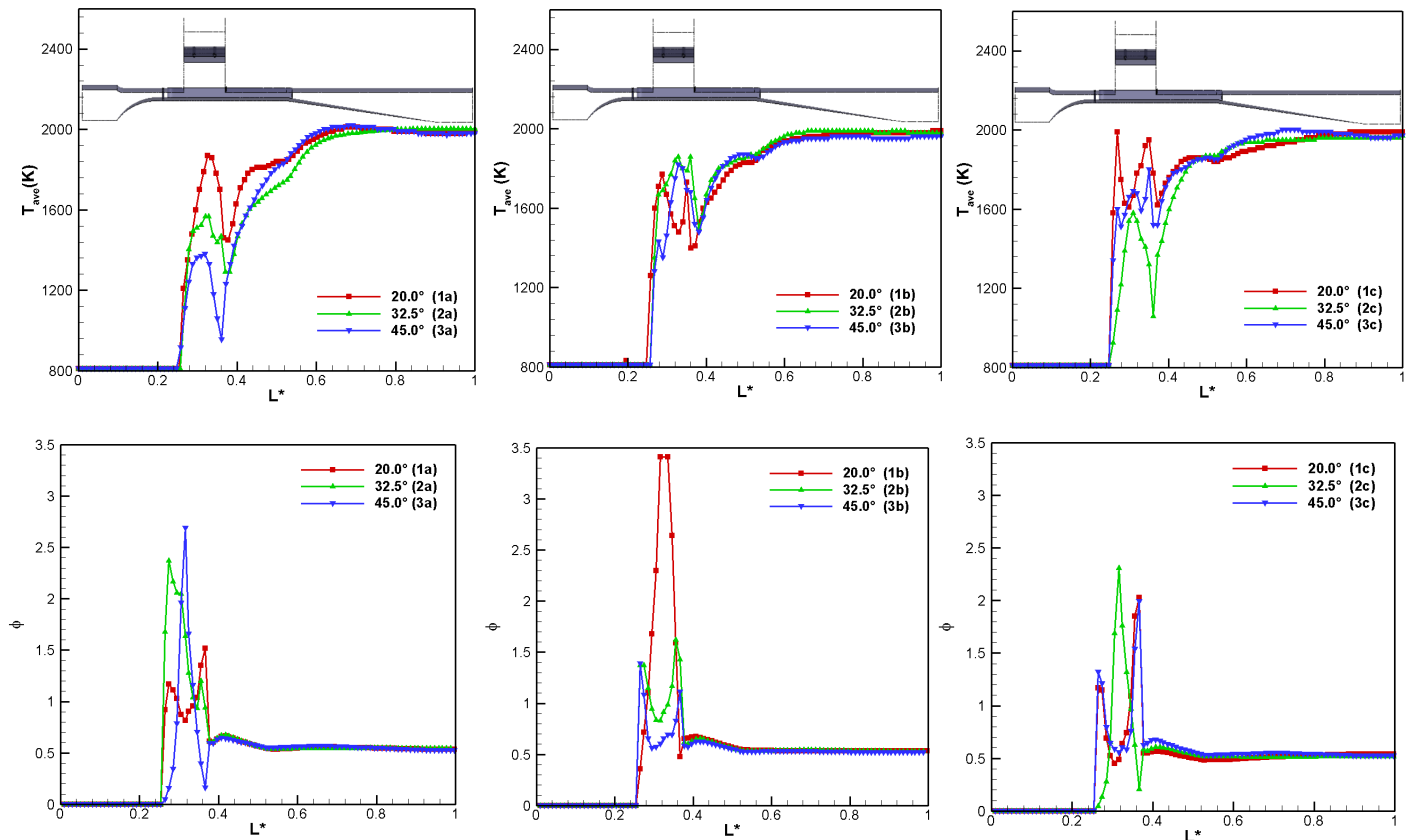


Figure 8. Axial Area-averaged Temperature and ϕ Profiles as a Function of Dimensionless Axial Position, L^* .

Effect of Centrifugal Force on Flame Length

Of great importance for the UCC-HGC design is to address the effect of centrifugal force on flame length. Here the flame surface is defined as the stoichiometric iso-surface holding combustion as shown in Figure 9. The iso-surfaces are colored by temperature. The results indicate that the flame extends from the CC driver jets towards the trailing edge of the IGV. It is important to note that even though the iso-surface is at constant equivalence ratio the temperature varies along the flame surface. Most flames are typically cooler at the CC, which is consistent with Figure 7 and Figure 8. Further downstream the temperature increases and it is maximum at

the tail of the flame front. This occurs because by varying the CC jet angle (α_{jet}) and/or $\dot{m}_{CC}/\dot{m}_{core}$ the stretch rate or scalar dissipation rate changes. These flame quenching effects are more pronounced in the CC than further downstream the CC. Hence, the CC flame temperature is lower than its corresponding equilibrium flame temperature.

Qualitatively, increasing the surface area and temperature of the flame that can be sustained within the CC leads to lower flame length. The converse is also true. Configuration 1c and 3b exhibit the shortest flame lengths. They achieve this by increasing their volume within the CC. Therefore, longer flames typically contained small flame volume within the CC. In terms of flame length as a function of α and $\dot{m}_{CC}/\dot{m}_{core}$ no definite pattern is observed.

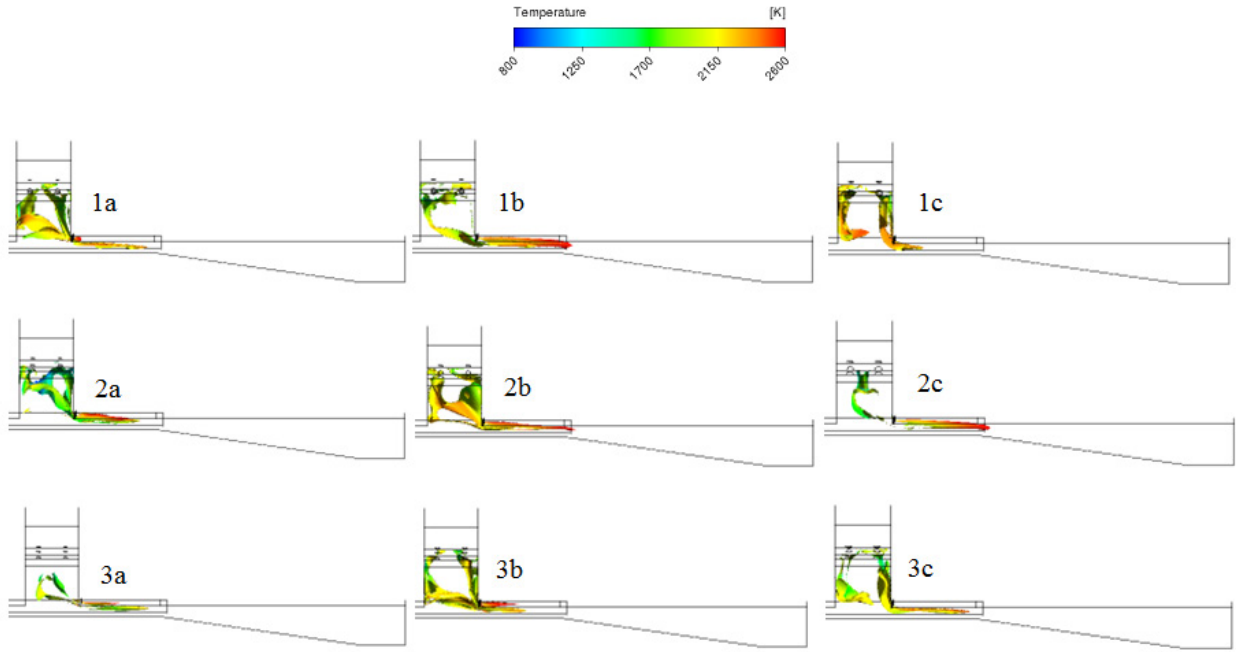


Figure 9. Side View of the Stoichiometric Iso-surface

(The iso-surface is clipped by $\tilde{C} \geq 0.5$ and colored by temperature (in Kelvin). The upstream portion of the UCC-HGC was truncated for convenience in this image.)

Effect of Centrifugal Force on g-loads and Turbulent Flame Speed

Since the design of this new rig that can operate at higher Mach number, higher operating pressures and higher inlet temperatures, while sacrificing centrifugal force, is based on non-reacting flow consideration it is vital to understand what the effect of combustion on the g-loads is. Figure 10 displays the area-averaged axial g-loads profiles for all reacting flow configurations under investigation. Important observations are as follows. First, the large g-load peaks at the CC are diminished at low $\dot{m}_{CC}/\dot{m}_{core}$ while enhanced at high $\dot{m}_{CC}/\dot{m}_{core}$ (cf. Figure 4 and Figure 10). Second, at intermediate CC-to-core air mass flow rates the g-loads are boosted at low α , while g-loads are weakened at high α_{jet} . Therefore, there is threshold dependent on $\dot{m}_{CC}/\dot{m}_{core}$ and α_{jet} at which CC g-loads are boosted or weakened. The g-loads are diminished because the velocity vector deflection occurs through the flame front. This, in turn, enhances the radial and axial velocity through thermal expansion, while reducing the magnitude of the tangential

velocity. On the contrary, when g-loads are enhanced the flame front is nearly perpendicular to the bulk swirl flow and the flame accelerates the velocity vectors primarily in the tangential direction. Third, configuration 1c reaches the maximum g-load, ca. 6000g, which is above its non-reacting value of 4500g. Similarly to non-reacting flow results which are very consistent with variations in CC jet angle (α_{jet}) and $\dot{m}_{CC}/\dot{m}_{core}$, the reacting flow results also very consistent. However, reacting flow results suggests that $\alpha_{jet}=20.0^\circ$ and $\alpha_{jet}=45.0^\circ$ are more sensitive to changes in $\dot{m}_{CC}/\dot{m}_{core}$ than $\alpha_{jet}=32.5^\circ$ is. In addition, high $\dot{m}_{CC}/\dot{m}_{core}$ is more sensitive to changes in α than lower $\dot{m}_{CC}/\dot{m}_{core}$ are.

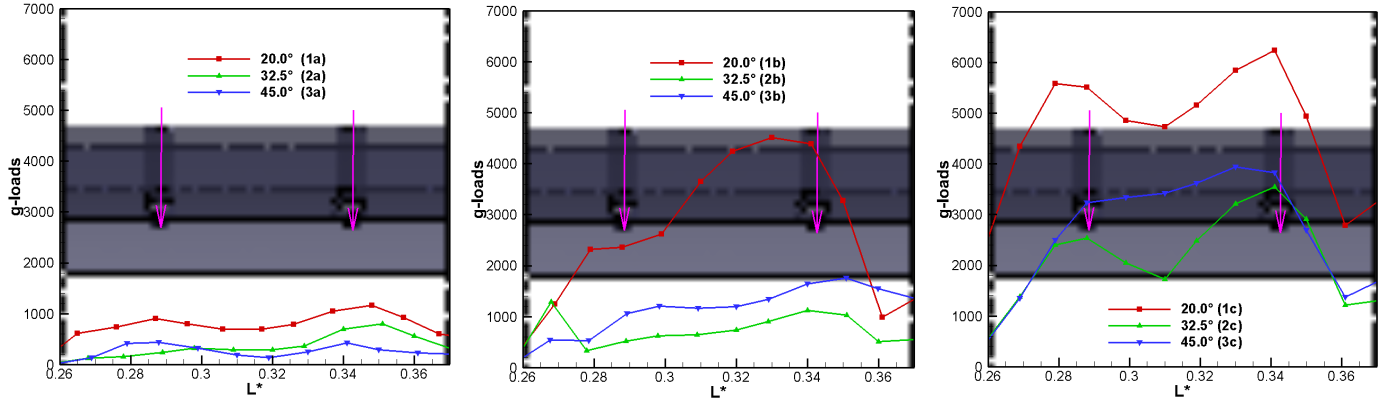


Figure 10. Area-averaged Axial g-loads Profiles as a Function of Dimensionless Axial Position, L^*
(The region of interest is from the CC forward wall to the CC aft wall. The magenta arrows indicate the location of the CC air driver jets.)

Turbulent flame speed has always been a major interest as discussed in the Introduction section. However, it is not easy to calculate it from very complicated geometry and turbulent partially premixed flames. Therefore, we indirectly examine the turbulent flame speed by inspecting the un-normalized reaction progress variable source term. If turbulent flame speed increases, then, the reaction progress variable, S_C , should also increase. Figure 11 illustrates the area-averaged axial S_C for all the configurations under investigation. Evidently, there are two regions of S_C . Low S_C occurs within the CC while very large S_C occurs immediately downstream the CC. This indicates that most of the reaction occurs outside the CC, which is consistent with Figure 7 and Figure 9. By comparing Figure 10 and Figure 11, it is suggested that the g-loads are enhancing S_C and potentially, turbulent flame speed, especially at high $\dot{m}_{CC}/\dot{m}_{core}$. This enhancement occurs through mean velocity gradients, which generate turbulent kinetic energy, that wrinkle or corrugate the flame surface area. This does not, however, necessarily mean that the turbulent flame speed is various factors greater than its corresponding turbulent flame speed given the same flow conditions. Nevertheless, S_C is lower in the CC than in the IGV passage plausibly because the stretch rates are high in the CC as indicated by high g-loads. Downstream of the CC the stretch rates are relatively low and S_C increases.

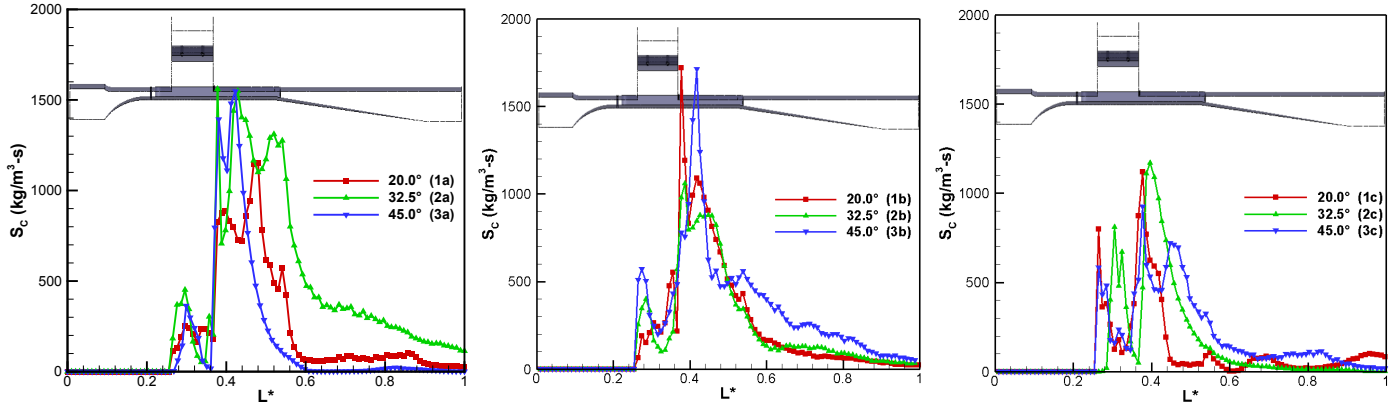


Figure 11. Area-averaged Axial S_c Profiles as a Function of Dimensionless Axial Position, L^* .

Effect of Centrifugal Force on Exit Temperature Profile

Finally, attainment of the desired temperature profile is of paramount importance because an adverse temperature profile can damage the turbine blades and deteriorate turbine performance. Since stresses are highest at the turbine hub and seal materials need to be protected at the turbine blade tip, the temperature profile needs to be center-peaked for modern high-performance engines [29]. Figure 12 shows that area-averaged radial temperature (T_{ave}) profiles just downstream of the IGV trailing edge. For series **a**, the best configuration is 1a, which has a CC jet angle (α_{jet}) of 20.0°. The exit temperature profile is nearly center-peaked. As the $\dot{m}_{CC}/\dot{m}_{core}$ or α_{jet} increases the center-peaked profile tends to deteriorate. The exit temperature profile is less sensitive to α_{jet} at high $\dot{m}_{CC}/\dot{m}_{core}$ than it is under low conditions. Similarly, exit temperature profiles are more sensitive to $\dot{m}_{CC}/\dot{m}_{core}$ at small α_{jet} than at large α_{jet} .

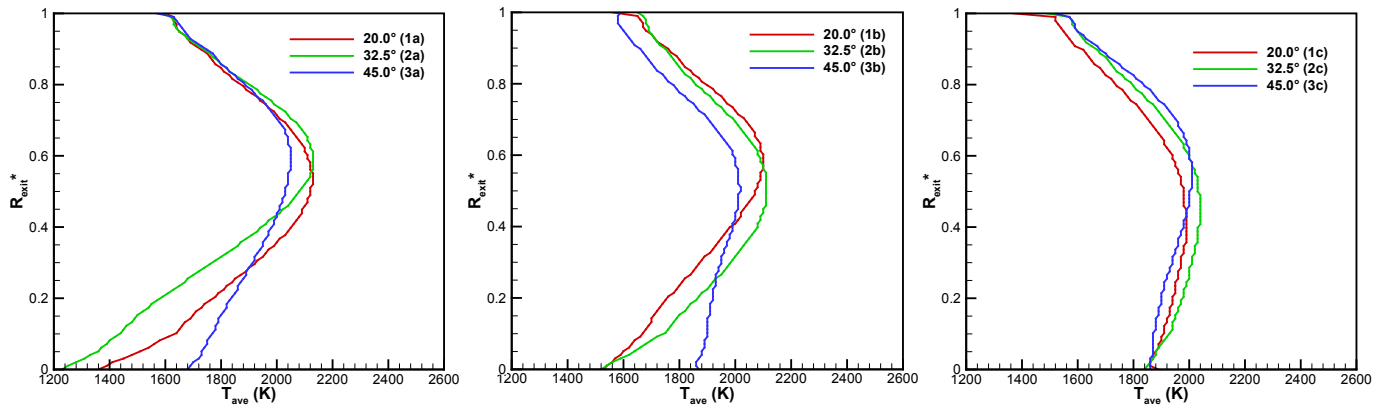


Figure 12. Area-averaged Radial Temperature (T_{ave}) Profiles just Downstream of the IGV Trailing Edge

(The profiles are for the configurations discussed in the context of Figure 5. The radial coordinate is dimensionless, R_{exit}^ .)*

2.1.10 Conclusions

A numerical investigation of reacting flows in an advanced high-g cavity, Ultra-Compact Combustor (UCC) concept is conducted. This UCC concept combines the primary and the dilution zones of a conventional combustor with high pressure turbine inlet guide vanes (IGVs) to shorten the length of the combustor compared to a conventional design with separate combustor and IGV components. The high-g cavity UCC (UCC-HGC) design uses high swirl in a circumferential cavity (CC) wrapped around a main stream annular flow. The high swirl is generated through angled CC driver jets, which, in turn, is based on the driver jet injection angle (α_{jet}) and the pressure drop across the driver jets. This centrifugal force is varied by changing the $\dot{m}_{CC}/\dot{m}_{core}$ and inclination angle (α_{jet}) relative to the cavity ring surface. Steady, rotational periodic, three-dimensional numerical simulations of this advanced combustor concept are performed following a multiphase, Reynolds-averaged Navier-Stokes (RANS), and nonpremixed flamelet (PVF) approach using FLUENT. Important conclusions are as follows.

1. Under non-reacting flow conditions the results for all configurations analyzed here are similar. The plenum feeds both the CC and the mainstream (core) flow. The driver jets imposed a very clear bulk swirl flow within the CC and the mainstream flow does not entrain into the CC. However, under reacting flow conditions the flame interacts with the flow and the bulk swirl flow is no longer very strong, especially at low CC-to-core air mass flow rates ($\dot{m}_{CC}/\dot{m}_{core}$) and larger α_{jet} . This is plausibly because the flame deflects the incoming driver jet flow, enhancing radial and axial velocity components through thermal expansion while diminishing the tangential component.
2. Under non-reacting flow conditions, the maximum g-load clearly decreases with increasing CC driver jet angle (α_{jet}). This effect becomes even more pronounced with increasing $\dot{m}_{CC}/\dot{m}_{core}$. Nonetheless, the g-loads are more sensitive to the increase in $\dot{m}_{CC}/\dot{m}_{core}$ than to the variation in α . On the other hand, under reacting flow conditions, the high CC g-loads are diminished at low $\dot{m}_{CC}/\dot{m}_{core}$ and large α_{jet} . Again, this is plausibly because the flame deflects the incoming driver jet flow. At high $\dot{m}_{CC}/\dot{m}_{core}$ and small α the g-loads are instead further enhanced beyond those exhibited under non-reacting flow conditions. This is possibly due that the flame is no longer deflecting the flow but instead it is accelerating in the tangential velocity because the flame is now more perpendicular to the bulk swirl flow. This is exciting because the g-loads do not necessarily decrease with reducing combustor size if large CC flow rates are applied.
3. Most flames are typically cooler inside the CC but further downstream the temperature increases and peaks at the flame tail. This suggests that flame quenching effects are more pronounced in the CC than in the mainstream. Qualitatively, increasing the surface area and temperature of the flame that can be sustained within the CC leads to lower flame length. The converse is also true. There appears to be negligible effect of $\dot{m}_{CC}/\dot{m}_{core}$ on flame length.
4. Even though g-loads appear to enhance reaction progress variable source (S_C) and, consequently, turbulent flame speed, this does not necessarily mean that the turbulent flame speed under g-loads exceeds its corresponding turbulent flame speed under 0 g's.
5. In terms of exit temperature profiles, the configuration that exhibits the best center-peaked profile is that at smallest α_{jet} and low $\dot{m}_{CC}/\dot{m}_{core}$. As the CC-to-core mass flow ratio or α_{jet} increases the center-peaked profile tends to deteriorate. The exit temperature profile is less sensitive to α_{jet} at high $\dot{m}_{CC}/\dot{m}_{core}$ than it is under low conditions. Similarly, exit temperature profiles are more sensitive to $\dot{m}_{CC}/\dot{m}_{core}$ at small α_{jet} than at large α_{jet} .

2.1.11 References

- [1] Burrus, D., Internal Communication, 2013
- [2] Briones, A.M., Sekar, B., Erdmann, T.J., "Effect of Centrifugal Force on Turbulent Premixed Flames," Eng. Gas Turbines Power, 2014; 137(1):011501-011501-10.
- [3] Briones, A.M., Sekar, B., Blunck, D.L., Erdmann, T.J., Shouse, D., "Reacting Flows in Ultra-Compact Combustors with Combined-diffuser-Flameholder," 2014, J. Prop. & Power, 1-15, 10.2514/1.B35141.
- [4] Lewis, G.D., Shadowen, J. H., Thayer, E.B., Swirling Flow Combustion, Journal of Energy, 1 (4): 201-205, 1977.
- [5] Lewis, G.D., Centrifugal-force Effects on Combustion, Proceedings of the Combustion Institute, 413-419, 1973.
- [6] Lewis, G.D., Combustion on a Centrifugal-force Field, Proceedings of the Combustion Institute, 625-629, 1971.
- [7] Katta, V.R., Blunck, D., Roquemore, W.M., Effect of Centrifugal Effects on Flame Stability in an Ultra-compact Combustor, AIAA 2013-1046.
- [8] Katta, V.R., Zelina, J., Roquemore, W.M., Numerical Studies on Cavity-Inside-Cavity-Supported Flames in Ultra Compact Combustor, Paper GT2008-50853, 2008.
- [9] Zelina, J., Sturgess, G. J., and Shouse, D. T., "The Behavior of an Ultra-compact Combustor (UCC) Based on Centrifugally-Enhanced Turbulent Burning Rates," 40th AIAA/ASME/SAE/ASEE Joint Propulsion Conference and Exhibit, AIAA Paper 2004-3541, 2004.
- [10] Zelina, J., Ehret, J., Hancock, R.D., Shouse, D.T., Roquemore, W.M., Sturgess, "Ultra-compact Combustion Technology using High Swirl for Enhanced Burning Rate," 38th AIAA/ASME/SAE/ASEE Joint Propulsion Conference & Exhibit, AIAA-2002-3725.
- [11] Zelina, J., Shouse, D.T., Neuroth, C., "High-pressure Tests of a High-g, Ultra-compact Combustor," 41st AIAA/ASME/SAE/ASEE Joint Propulsion Conference & Exhibit, AIAA-2005-3779.
- [12] ANSYS Inc., ANSYS FLUENT THEORY GUIDE 15.0, 2014.
- [13] Kader, B., Temperature and Concentration Profiles in Fully Turbulent boundary Layers, International Journal of Heat and Mass Transfer, 24(9):1541-1544, 1981.
- [14] Barth, T.J., Jespersen, D., The Design and Application of Upwind Schemes on Unstructured Meshes, Paper AIAA-89-0366, January, 1989.
- [15] Anderson, W., Bonhus, D.L., An Implicit Upwind Algorithm for Computing Turbulent Flows on Unstructured Grids, Computers Fluids, 23(1):1-21, 1994.
- [16] Briones, A.M., Thornburg, H., Sekar, B., Neuroth, C., Shouse, D., "Numerical-Experimental Research of Ultra Compact Combustors containing Film and Effusion Cooling," AIAA-2013-1045, 51st AIAA Aerospace Science Meeting, Grapevine, TX, 2013.
- [17] Briones, A.M., Sekar B., Thornburg, H., "Modeling and Simulation of Enhanced Reactant-Product Mixing in Ultra Compact Combustors," 48th AIAA/ASME/SAE/ASEE Joint Propulsion Conference & Exhibit and 10th International Energy Conversion Engineering Conference, 30 July - 1 August, Atlanta, GA, 2012.
- [18] Pitsch, H., Barth, H., Peters, N., Three-Dimensional Modeling of NOx and Soot Formation in DI Diesel Engines Using Detailed Chemistry Based on the Interactive Flamelet Approach, SAE-962057, 1996.
- [19] Pitsch, H., Peters, N., A Consistent Flamelet Formulation for Non-Premixed Combustion Considering Differential Diffusion Effects, Combustion and Flame. 114. 26-40. 1998.
- [20] Sirjean, B., Dames, E., Sheen, D.A., You, X.-Q., Sung, C., Holley, A.T., Egolfopoulos, F.N., Wang, H., Vasu, S.S., Davidson, D.F., Hanson, R.K., Bowman, C.T., Kelley, A., Law, C.K., Tsang, W., Cernansky, N.P., Miller, D.L., Violi, A., Lindstedt, R.P., A High-Temperature Chemical Kinetic Model of N-alkane Oxidation, JetSurF version 1.0, September 15, 2009 (<http://melchior.usc.edu/JetSurF1.0>).
- [21] Briones, A.M., Thornburg, H., Sekar, B., Neuroth, C., Shouse, D., "Numerical-Experimental Research of Ultra Compact Combustors containing Film and Effusion Cooling," AIAA-2013-1045, 51st AIAA Aerospace Science Meeting, Grapevine, TX, 2013.
- [22] Briones, A.M., Sekar B., Thornburg, H., "Modeling and Simulation of Enhanced Reactant-Product Mixing in Ultra Compact Combustors," 48th AIAA/ASME/SAE/ASEE Joint Propulsion Conference & Exhibit and 10th International Energy Conversion Engineering Conference, 30 July - 1 August, Atlanta, GA, 2012.
- [23] CHEMKIN-PRO 15113, Reaction Design: San Diego, 2012.
- [24] Hirschfelder, C.F., Curtiss, Bird, R.B., Molecular Theory of Gases and Liquids, John Wiley, New York, 1954.
- [25] Warnatz, J., Influence of Transport Models and Boundary Conditions on Flame Structure, Friedr., Vieweg, Wiesbaden, 1982.
- [26] Kee, R.J., Coltrin, M.E., Glarborg, P., Chemically Reacting Flow, Wiley-Interscience, New Jersey, 2003.
- [27] Wilke, C.R., A Viscosity Equation for Gas Mixtures, J. Chem. Phys., 18:517-522, 1950.
- [28] McBride, B.J., Gordon, S., Computer Program for Calculating and Fitting Thermodynamics Functions, NASA Reference Publication 1271, 1992
- [30] Lefebvre, A.H., Gas Turbine Combustion, Taylor&Francis, 1983.

2.2 Influence of Fuel Characteristics on the Prediction of Lean Blowout in Bluff-body Stabilized Flames

2.2.1 Introduction

Gas turbine engines, both in ground-based industrial settings and in aviation settings, utilize bluff-body stabilized flames, often running at lean fuel-air ratios to extend the lifetime of the equipment or to comply with emissions regulations. However, running the equipment at a lean condition also puts the system at risk for lean blowout, which can result in facility inefficiencies, hardware damage, and a catastrophic reduction in aircraft performance. For this reason understanding lean blowout and predicting its occurrence is critical for the operability of these systems.

Some of the first experimental studies of lean blowout behavior in bluff-body stabilized flames were conducted by Williams [1] in the late 1940s and DeZubay [2] in the 1950s. DeZubay's work, stemming from experiments conducted on disk-shaped flameholders, focused on correlating the fuel-to-air ratio at lean blowout with a parameter based on the inlet pressure and velocity and the characteristic diameter of the flameholder. In his original work in 1950, DeZubay did not vary the inlet temperature of the rig; therefore, a modified DeZubay correlation that includes temperature dependence has become more widely used, with T representing the temperature parameter:

$$DeZ_T = \frac{U * 10^4}{P^{0.95} D^{0.85} T^{1.2}} \quad (13)$$

In this correlation, velocity (U) is in ft/s, pressure (P) in psi, diameter (D) in inches, and temperature (T) in Rankine. Although DeZubay's experiment included both rich and lean blowout, the correlation is intended only for the lean region of the stability curve. Figure 1 shows the DeZubay curve as constructed from the data used for the present work.

While the DeZubay curve is a well-known and popular correlation, Figure 1 demonstrates some of its drawbacks. At a given DeZubay number, the equivalence ratio at lean blowout can vary greatly. For example, at a DeZubay number near 6000, the equivalence ratio at lean blowout ranges from 0.28 up to 0.75. In addition, there appears to be a fuel effect that the correlation does not capture. The propane data follow a curve reasonably well, as indicated by the black line in Figure 1. However, data from experiments run on JP-4, methane, gasoline, and jet fuels 7721, 6308, and 6169 follow different patterns. The AFRL jet fuel data is new data from the current study.

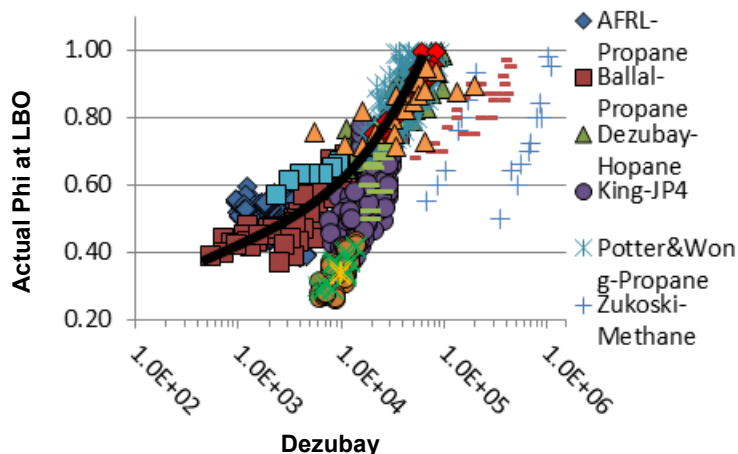


Figure 13. Dezubay Correlation with Data from Present Work

Following DeZubay's work the lean-blowout behavior of bluff-body stabilized flames continued to be studied by numerous researchers, including King [3], Zukoski and Marble [4, 5], Ozawa [6], Ballal and Lefebvre [7], and Plee and Mellor [8]. Most researchers agreed that lean blowout was governed by a competition between the chemical and fluid-mechanic timescales, which can be ratioed to yield what is known as a Damköhler number. However, researchers have debated which timescales are critical to the lean blowout process.

According to Zukoski and Marble [5], active combustion in the region of the recirculation zone is limited to its shear-layer boundaries, with a portion of the hot products being re-entrained into the recirculation zone. In a stable flame, the fresh gas flowing past the bluff body is ignited before it reaches the end of the recirculation zone, propagating the flame. Zukoski and Marble theorize that when the fresh gas fails to mix with the hot products in the recirculation zone for an adequate period of time, the flame will blow off. They identified the time that the fresh gas spends in the shear layer and the ignition delay time as the critical timescales in the blowout process. They also identified the ratio of the free-stream velocity and the length of the recirculation zone as being representative of the time that the fresh gas spends in contact with the hot combustion products.

Plee and Mellor [8] also developed a model to explain lean blowout that was based on the various timescales involved, including fluid-mechanic and chemical times as well as droplet-evaporation time and fuel-injection mixing time in the case of heterogeneous mixing. The fluid-mechanic timescale was taken to be the turbulent mixing time in the shear layer between the relatively cold incoming reactants and the hot, burned gases in the recirculation zone. This timescale was approximated as the ratio of the flameholder width, which was also considered to be a measure of the size of the recirculation zone, and the velocity of the incoming gas at the lip of the flameholder. The ignition delay time was taken to be the critical chemical timescale. The model developed by Plee and Mellor successfully collapsed the lean-blowout data from Ballal and Lefebvre [7] to a straight line.

Radhakrishnan et al. [9] developed a correlation for the blowout velocity of premixed, bluff-body stabilized turbulent flames by examining the relevant turbulent and chemical timescales, using a model of turbulence where small-scale structures are actually similar to tubes of

vorticity. Radhakrishnan et al. argued that the Taylor microscale is the scale across which the flame must propagate at the laminar flame speed, S_L , and that for the flame to remain stable, the laminar flame propagation must occur in a time less than the characteristic fluid-mechanic time. Based on previous studies, including those of Plee and Mellor [8], Radhakrishnan et al. [9] took the shear-layer mixing time to be the critical characteristic turbulent timescale rather than the residence time in the recirculation zone.

Assuming isotropic turbulence and that the turbulence intensity is proportional to the velocity at the flameholder lip (U_{lip}), and the integral length scale of a single eddy is proportional to the length of the recirculation zone (L), Radhakrishnan reduced the Damköhler number to Eq 14, where ν is the kinematic viscosity, τ_c the chemical timescale, τ_e the eddy (fluid mechanic) timescale, and S_L the laminar flame speed.

$$\tau_c / \tau_e = \left(\frac{U_{lip} \nu}{L} \right)^{1/2} (S_L)^{-1} \quad (14)$$

Using Eq 14 as well as empirical correlations to estimate the laminar flame speed, Radhakrishnan et al. [9] developed a model for the blowout velocity of bluff-body stabilized flames that correlated well with experimental data obtained on lean propane flames. The lip velocity was found to be a better parameter for determining stability than the gas inlet velocity. In addition, the recirculation zone length was found to be a more appropriate length scale than the flameholder size, although the authors acknowledged the difficulties in measuring the recirculation zone length.

Kariuki et al. [10] developed a parameter based on the work of Radhakrishnan et al. [9] and then plotted this value against the flame power for swirl-stabilized flames; they found that the scatter was “considerably smaller” than that usually observed in the literature.

Research conducted by Lieuwen and colleagues [11-13] has also been focused on the mechanism of lean blowout and the timescales that may be critical to the process. Nair et al. [11] conducted laser-sheet imaging studies and velocity-field measurements using particle image velocimetry (PIV) to determine the transient dynamics of bluff-body stabilized flames near blowout. They found that the first stage of blowout was characterized by localized “holes” in the flame sheet where the instantaneous stretch rate exceeds the extinction stretch rate. As the equivalence ratio decreased from this condition, the duration and scale of these “holes” increased. The authors argued that as blowout was approached, the flame entered a second stage of blowout where large-scale, violent flapping of the flame front was noted, similar to von Karman-type shedding. They suggested that the possible mechanism for blowout is the introduction of a “slug” of relatively cool, unreacted mixture into the recirculation zone by the large-scale dynamics observed in the second stage. This “slug” would then fail to ignite the incoming mixture, and the flame would blow out. Chauduri et al. [14] noted a similar progression of flame behavior near blowoff, where shear-layer extinction and recirculation zone burning are precursors to blowoff for premixed flames.

Husain [12] attempted to develop a Damköhler number that could adequately model lean blowout in a large set of data obtained from past and recent literature, noting that almost every past researcher has concluded that a competition between some fluid-mechanic timescale and a

chemical timescale is critical in explaining the blowout process. Using CHEMKIN software, Husain calculated the minimum residence time of a well-stirred reactor for which a majority of the reactants are consumed (τ_{PSR}) and used this as the chemical timescale in the Damköhler number. For the fluid-mechanic timescale, Husain assumed D/U , where U is the lip velocity, and D is the characteristic diameter of the bluff body. Husain claims a “reasonable grouping” of the data based on a plot of his Damköhler number as a function of Reynolds number, and that the Damköhler number shows variation with Reynolds number. However, the dependence on Reynolds number is clearer within a few individual datasets than the data set as a whole, and the plot itself is on a log scale.

While bluff-body flames have been studied extensively for decades, a consensus on the physical and chemical processes that lead to blowout has not been reached. The conclusions of Shanbhogue et al. [13] imply that the mechanism relies on ignition processes. Both Radhakrishnan et al. [9] and Kariuki et al. [10] had some success correlating the equivalence ratio at blowout to flame speed, which would suggest that blowout is not governed by the ignition timescales. Shanbhogue et al. [13] also suggest that as the flame nears blowout, it develops a sinuous instability, which entrains cold reactants into the flame, disrupting the ignition process. However, it is unclear whether all bluff-body flames exhibit this sinuous structure before blowout or whether it has a primary influence on the blowout. For example, Khosla et al. [15] performed a large eddy simulation (LES) analysis on bluff bodies with and without small tabs. The tabs effectively broke up the von Karman vortex shedding, and yet both flameholders blew out at the same premixed equivalence ratio. In addition, a study by Huelskamp et al. [16] evaluated the effect of shape on blowout by correlating the cold-flow Strouhal number of various bluff-body shapes to the equivalence ratio at lean blowout. The Strouhal number did not appear to have a first-order effect on lean blowout, indicating that the shape and the vortex shedding behavior did not govern the mechanism of blowout.

The present work employed experimental data taken at the Air Force Research Laboratory and that collected from many of the papers reviewed above to develop a correlation for predicting lean blowout using a least-squares curve-fit method. The laminar flame speed and ignition delay time were calculated for current experimental conditions as well as for selected data sets from the literature using the chemical kinetics software Cantera, and the results were incorporated into the correlations.

This study will serve two purposes: 1) to provide an accurate, practical method of predicting lean blowout for designers and modelers and 2) to provide insight into the critical parameters and timescales that govern the blowout process by examining the significance of each parameter included and the physical and chemical processes that it may affect.

2.2.2 Experimental Setup

Experiments were performed in two combustion laboratories at the Air Force Research Laboratory (AFRL) at Wright-Patterson Air Force Base. Bluff-body flameholding tests were initially performed in an atmospheric-pressure combustion facility using propane as a fuel. The facility can deliver air inlet temperatures of up to 500 K with four electric heaters with a total power capacity of 358 kW. Inlet temperatures of up to 1000 K can be achieved with vitiation. Air is metered through orifice plates with an uncertainty within 2%, and coriolis meters measure the fuel flow within 0.35% of total flow.

The available airflow to this facility can provide lip Mach numbers of up to 0.3 and lip Reynolds numbers up to 100,000 in a test section that is 15.2 cm high by 12.7 cm wide. Lip Reynolds number is calculated using the flameholder diameter and the velocity of the incoming gas as it passes over the flameholder. Figure 14 is a schematic of the test rig with a v-gutter bluff body installed. The airflow is left to right and passes through a perforated plate, which provides more uniform velocity and temperature profiles at the inlet of the test section.

The flameholder trailing edge was 58 cm from the inlet of the test section. The flameholder spans the full height of the rig, and optical access through quartz windows is available for high-speed imaging. Gaseous propane is premixed with the air ~ 150 cm upstream of the test section. The fuel distribution was validated using acetone-seeded planar laser-induced fluorescence (PLIF). The fuel-air mixture is ignited with an ethylene torch behind the bluff body. Figure 15 shows the rig as it is installed in the facility.

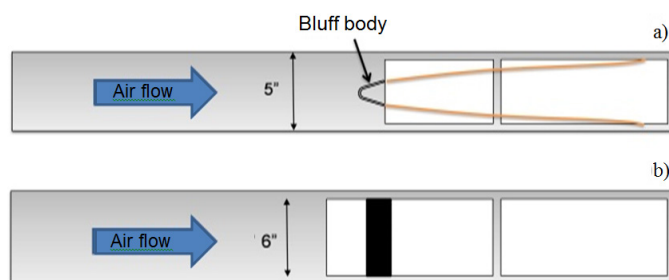


Figure 14. Atmospheric Pressure Combustion Rig Configuration, (A) Top View; (B) Side View

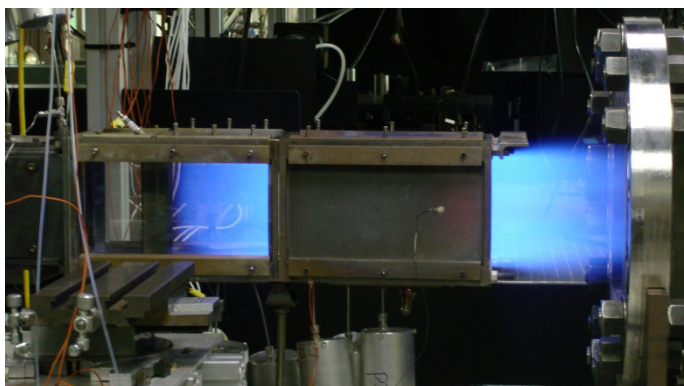


Figure 15. Atmospheric Pressure Combustion Rig

Experiments for this study were also performed in the High Pressure Combustion Research Facility. Various jet fuels, including petroleum-derived JP-8, tallow-derived hydro-treated renewal jet (HRJ) fuel, and camelina-derived HRJ fuel, were combusted in a vitiated stream. The molecular weight and hydrogen-to-carbon ratios of these fuels were measured by Princeton University [17].

Table 3. Correlations Considered in This Study

Reference	Lip Velocity (m/s)	Flame-holder Diameter (cm)	Inlet Temperature (K)	Inlet Pressure (atm)	Reynolds Number	Fuel Type
Huelskamp et al.	6.40-52.1	0.95-3.8	290-574	0.98	4800-86,000	Propane
Ballal and Lefebvre	10.3-151	2.0-12.5	300-575	0.20-0.99	12,000-506,000	Propane
DeZubay	26.2-215	0.64-2.5	306	0.20-1.0	4200-345,000	Hopane
King	122-226	3.8	700-1033	0.35-0.85	14,000-87,000	JP-4
Potter and Wong	24.1-233	0.95-2.5	300-306	0.25-0.94	7,300-260,000	Propane
Williams	8.84-108	0.25-1.3	300	1.0	1,400-89,000	Propane
Zukoski	24.7-368	0.025-0.64	339-478	1.0	200-57,000	Methane Gasoline
Chaudhuri et al.	20.1-39	0.95	285-295	1.0	13,000-25,000	Propane
Yamaguchi	9.14-38.1	2.4	293	1.0	14,000-60,000	Propane
Barrere	11.9-47.9	0.50	290	1.0	4,000-16,000	Propane
AFRL (current)	72.8-149	3.8	732-920	0.68	20,000-53,000	Jet fuels

The test section is 15.2 cm wide and 22.9 cm tall with a 3.8-cm-wide v-gutter, and Mach numbers up to 0.3 can be achieved. In this facility, the pressure in the test section can be varied from 0.34 to 1.4 atm. Heaters provide inlet air temperatures of up to 670 K, and vitiation can raise the test section inlet temperature to 1000 K. Oxygen levels of the gas entering the test section can be varied from 17 to 21%, depending on the chosen level of vitiation; for this study, the points chosen were taken at an oxygen level of ~18%. The test section fuel is injected ~51 cm upstream of the flameholder through atomizing nozzles, providing a premixed, pre-vaporized fuel condition. The fuel distribution, which was approximately uniform over the cross-section, was verified using PLIF. No liquid droplets were observed in the PLIF plane near the inlet of the test section. The molecular weight of the jet fuels ranged from 153.9 to 161 g/mol, and the hydrogen-to-carbon ratio of the jet fuels ranged from 2.017 to 2.176.

Lean-blowout measurements were conducted on four types of stainless-steel bluff-body flameholders: v-gutters with diameters of 0.95 – 3.8 cm, a cylinder, a plate, and a square cylinder. The cylinder, plate, and square cylinder were 3.8 cm wide. Blowout was achieved by first reaching the desired inlet conditions and then decreasing the fuel flow until the flame was very near blowout but stable. The fuel flow was then decreased slowly until the flame blew out, and a data point was recorded.

Correlation Setup

The data points from these experiments were combined with data points obtained from the publications of other authors, including Ballal and Lefebvre [7], DeZubay [2], King [3], Potter and Wong [18], Williams [1], Zukoski [4], Chauduri [14], Yamaguchi [19], and Barrere [20]. Table 1 provides a summary of the experimental parameters from each study. Hopane, the fuel

shown for the DeZubay work, contained 95% propane and 5% butane and/or ethane. The jet fuels used for the AFRL dataset were Fuel 6169, a petroleum-derived JP-8.

Fuel 6308, a tallow-derived HRJ fuel, and Fuel 7721, which is a 50-50 blend of 6169 and a camelina-derived HRJ fuel. An input file of more than 1100 individual points included the relevant parameters from each study, such as inlet conditions and flameholder characteristics. The least-squares curve-fit function in the Matlab optimization toolbox was used to find an optimal correlation. The desired equation form was selected before running the correlation code.

In order to evaluate how various parameters increased or decreased the effectiveness of the correlation, the adjusted R-squared value for each correlation was calculated according to Eq. 15.

$$R_{adj}^2 = 1 - \frac{SS_E / (n - p)}{SS_T / (n - 1)} \quad (15)$$

In this equation SS_E is the sum of the squares of the residuals, SS_T the total sum of the squares of the original dataset, n the number of data points, and p the number of parameters used in the correlation.

The adjusted R-squared statistic is more appropriate than the traditional R-squared statistic for comparing correlations that contain varying numbers of parameters. A least-squares curve-fit algorithm will run until the residuals have been reduced as much as possible. If a parameter is introduced that is not relevant to the correlation, the curve fit will simply reduce its significance until it is negligible, and the change to the goodness of fit for that correlation will remain unchanged. If the parameter is relevant, the optimization process will assign an appropriate factor such that the goodness of fit should improve. Because the least-squares algorithm will always reduce the residuals as much as possible, introducing a new parameter should never worsen the fit, and will therefore never decrease the traditional R-squared value. The adjusted R-squared statistic penalizes added parameters to correct for this bias, providing a better statistic for comparing correlations [21]. All R-squared statistics reported throughout this work will be the adjusted R-squared values.

In addition to calculating the R-squared statistic, the residual for each point was plotted against the predicted equivalence ratio at lean blowout to determine whether trends were present within the residuals. If trends are present, it indicates that the model is inadequate, possibly due to phenomena that are not fully captured in the correlation [21]. For the correlations in this study, the residuals were randomly distributed over the range of predicted equivalence ratios.

Cantera [29] was used to calculate the laminar flame speeds and ignition delay times for selected data. Two hundred data points over a range of pressures, temperatures, velocities, Reynolds numbers, and flameholder geometries were selected from the blowout experiments on propane and methane for the laminar flame speed computation. Propane and methane were chosen because chemical mechanisms that are validated at relevant conditions for these fuels are readily available. The GRI-Mech 3.0 [22] mechanism was used for the methane chemistry, and a mechanism developed by Gokulakrishnan et al. [23] was used for the propane chemistry. GRI-Mech 3.0 is an optimized mechanism designed to model natural-gas combustion with 53 species and 325 reactions [22], while the detailed propane mechanism [23] consists of 136 species and 966 reactions. The propane mechanism has been validated against experimental data at

temperatures pertinent to the present study (300 – 650 K), as shown in Figure 4 [23]. Cantera was employed to calculate the laminar flame speed using the inlet conditions at each data point. For the data evaluated, the flame speeds ranged from 6.73 to 55.11 cm/s. These data were then processed through the Matlab optimization toolbox in a manner similar to that described previously.

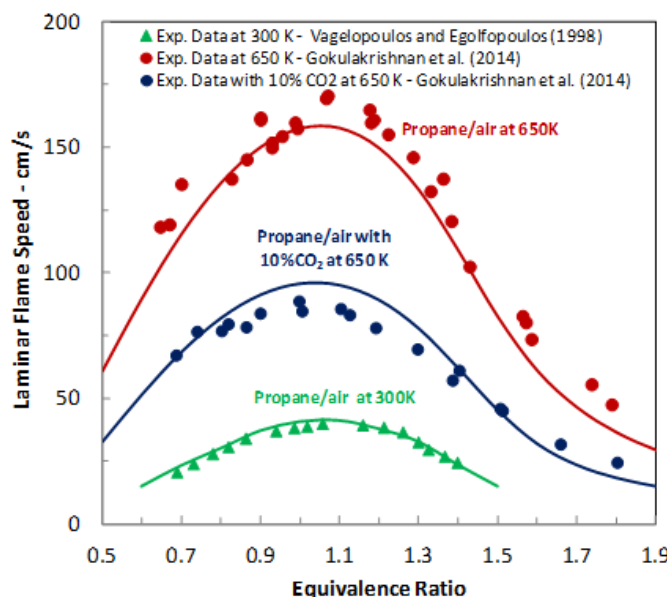


Figure 16. Validation of Cse Propane Mechanism against Flame Speed Experimental Data [23]

Since methane and propane have long ignition delay times at atmospheric pressure and relatively low temperature (below 600 K), the dataset for jet fuels was selected to investigate the blowout correlation with ignition delay time. A detailed surrogate kinetic mechanism developed by Gokulakrishnan et al. [30] was used to compute the ignition delay time of jet fuels. This mechanism uses a surrogate mixture for each jet fuel composed of n-dodecane, n-decane, iso-octane, and propyl-benzene. The ratio of the various components is determined by matching the molecular weight, hydrogen-to-carbon ratio, derived cetane number, and threshold sooting index of the target fuel. Surrogates that mimic these global fuel properties exhibit chemical kinetics-related behavior very similar to that of the target fuels they are meant to emulate [24, 25]. The ignition delay time was calculated for each point based on its inlet conditions using Cantera [29]. The oxidizer composition was calculated using a Matlab function that relies on combustion chemistry and thermodynamic principles of equilibrium to calculate the chemical make-up of the inlet gases after vitiation. The Matlab least-squares curve-fit function then used the resulting data to find the desired correlation. For the data evaluated, the ignition delay times ranged from 412 to 5728 ms.

2.2.3 Correlation Results

In a previous study of Huelskamp et al. [16], a portion of the current dataset was used to explore which flow parameters and dimensionless numbers were relevant in a correlation for predicting lean blowout. The smaller dataset did not account for vitiation effects, nor did it include the alternative jet fuel data. Because this work found the most relevant parameters to be lip velocity, flameholder diameter, pressure, and temperature, these were the initial factors considered in the

present analysis. In addition, it was found that employing a ratio of lip velocity to flameholder diameter instead of using each factor individually was only slightly detrimental to the goodness of fit of the correlation, and this ratio is recognized as a fluid-mechanic timescale. As such, a ratio of the two values is used in the following correlations. In these correlations, velocity (U) is in m/s, pressure (P) in atm, diameter (D) in m, and temperature (T) in K.

Figure 17 shows the correlation results with all of the available data. The data are plotted with the predicted equivalence ratio (or phi) at lean blowout (LBO) on the x-axis and the actual equivalence ratio at lean blowout on the y-axis. The black line running through the plot represents a “perfect” correlation (i.e., the predicted phi at LBO is equal to the experimental phi at LBO). The plot legend indicates the fuel used in each experiment. Equation 16 is the correlation equation. The R-squared value from this correlation is 0.852.

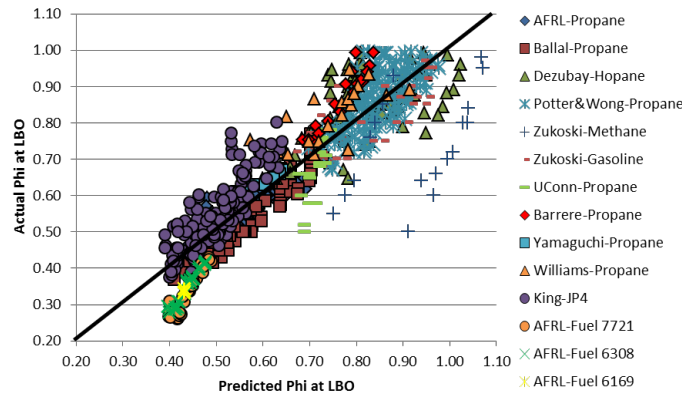


Figure 16. Correlation Results with D/U, Temperature, and Pressure as Factors ($R^2=0.852$)

$$\phi_{predicted} = \frac{4.864}{\left(\frac{D}{U}\right)^{0.1438} P^{0.2734} T^{0.5430}} \quad (16)$$

Despite the relatively good fit of the data to the correlation equation, some effects are visibly not captured. Close examination of Figure 5 reveals that data points obtained from experiments using fuels other than propane appear either to fall away from the “perfect-fit” black line, as in the case of methane and alternative jet fuel data, or to follow a slightly different slope on the plot, as in the case of the JP-4 data. This observation led to exploring the addition of fuel characteristics to the correlation.

As discussed in the Experimental Setup Section, researchers have successfully developed surrogate jet fuel formulations based on molecular weight, hydrogen-to-carbon ratio, threshold sooting index (TSI), and derived cetane number (DCN) [24, 25]. Of these parameters, both molecular weight and hydrogen-to-carbon ratio are easily obtained for all of the fuels in the dataset for this study; therefore, the molecular weight (MW) and hydrogen-to-carbon ratios (H/C) for each fuel were added to the correlation. The parameters were added separately so that the effect of each could be discerned.

Figure 18 displays the data plotted after adding the fuel molecular weight to the correlation equation, as shown in Eq 17.

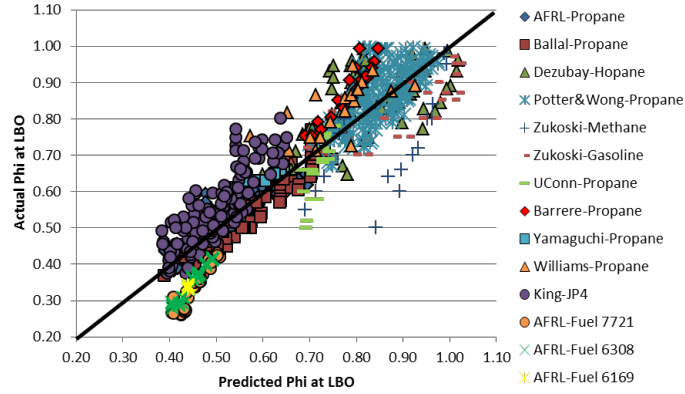


Figure 17. Correlation Results with Molecular Weight as Fuel Factor ($R^2=0.858$)

$$\phi_{predicted} = \frac{5.564 \times MW^{0.0834}}{\left(\frac{D}{U}\right)^{0.1479} P^{0.2687} T^{0.6269}} \quad (17)$$

The R-squared value from this correlation is slightly higher than that from the correlation without molecular weight, increasing the value by 0.006. The exponent on molecular weight in the correlation is also quite small. Examination of Figure 6 shows that the only readily apparent benefit of the additional parameter is to bring the Zukoski methane data [4] closer to the perfect fit-line. The Zukoski gasoline data [4] and the AFRL jet fuel data actually appear to drift farther from the perfect-fit line with the addition of molecular weight in the correlation.

Figure 19 shows the data plotted with the addition of the hydrogen-to-carbon ratio of each fuel to the correlation equation, shown in Eq. 18. The R-squared value of the correlation is 0.861, which is higher than the R-squared value of the correlation with molecular weight and the R-squared value of the initial correlation, 0.852. The addition of the hydrogen-to-carbon ratio appears to bring the methane data closer to the perfect-fit line and does not have the negative influence that the molecular weight had on the AFRL jet fuel data.

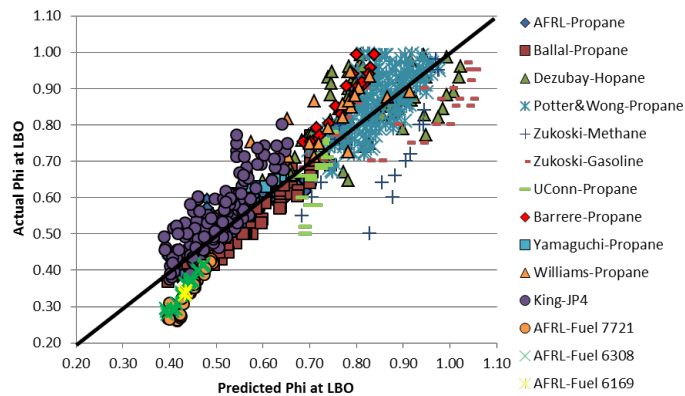


Figure 18. Correlation Results with Hydrogen-to-Carbon Ratio as Fuel Factor ($R^2=0.861$)

$$\phi_{predicted} = \frac{8.231}{\left(\frac{D}{U}\right)^{0.1438} P^{0.2732} T^{0.5973} \left(\frac{H}{C}\right)^{0.2201}} \quad (18)$$

Although the addition of the hydrogen-to-carbon ratio improves the R-squared value and brings the methane data closer to the perfect-fit line, the AFRL jet fuel data continue to diverge from the perfect fit. The AFRL jet fuel data as well as King's JP-4 data [3] were obtained in vitiated flows. Vitiation introduces a variety of chemical species that can affect the combustion reaction and, in turn, the Damköhler number and the lean-blowout process. In addition, vitiation reduces the amount of oxygen available in the combustion reaction. Researchers have found that vitiation results in higher equivalence ratios at lean blowout because of decreased reactivity from reduced oxygen levels [26].

In an attempt to capture these effects, the vitiation level was included in the correlation by calculating the percentage of oxygen in the oxidizing gas using the Matlab combustion chemistry code discussed previously. In the case of the AFRL data, this calculation could be done directly using actual air and fuel flows recorded by the combustion facility. The oxygen level for King's data was obtained by varying the vitiator fuel-air ratio in the code until the gas temperature matched that of the inlet temperature reported by King [3]. The correlation was then run again with both the oxygen level and the hydrogen-to-carbon ratio included. Figure 20 shows the data plotted with the new correlation; the correlation equation is shown in Eq. 19. The R-squared value of the correlation has improved to 0.873, from a previous value of 0.861. The AFRL jet fuel data has moved closer to the perfect-fit line.

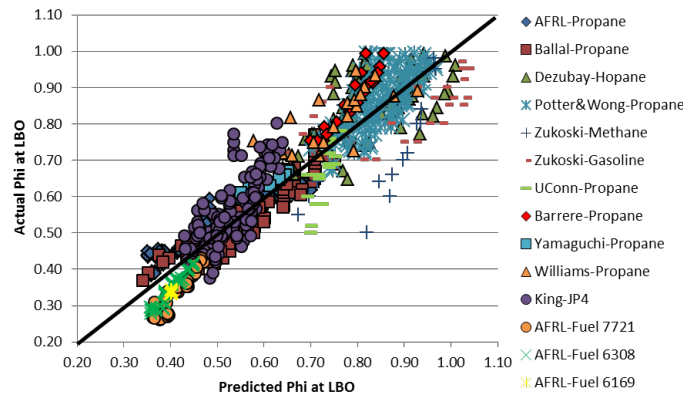


Figure 20. Correlation Results with H/C and Oxygen Content, ($R^2=0.873$)

$$\phi_{predicted} = \frac{1.02 \times 10^3}{\left(\frac{D}{U}\right)^{0.1464} P^{0.2612} T^{0.8416} \left(\frac{H}{C}\right)^{0.2130} O_2^{1.131}} \quad (19)$$

2.2.3.1 Correlation with Laminar Flame Speed

Cantera was used to calculate the laminar flame speeds for 200 data points taken on propane and methane over a range of pressures, temperatures, velocities, Reynolds numbers, and flameholder geometries. These data were then processed with the Matlab optimization toolbox to investigate the effect of laminar flame speed on blowout. Adjusted R-squared values were also calculated.

As discussed previously, Kariuki et al. [10] proposed the use of the parameter in Eq. 20 to predict when lean blowout will occur. This parameter is derived from a rearrangement of the turbulent premixed flame extinction theory originally proposed by Radhakrishnan et al. [9]. In

Eq (8), U_b is the bulk velocity, d the flameholder diameter, S_L the laminar flame speed, and ν the kinematic viscosity of the reactants.

$$\left[\left(\frac{U_b}{d} \right) \left(\frac{\nu}{S_L^2} \right) \right]^{1/2} \quad (20)$$

Kariuki et al. [10] plotted this value against the flame power for swirl-stabilized flames and found that the values for premixed flames were near unity. The dataset for which laminar flame speed was calculated in the current study was used in an attempt to verify the results of previous researchers. Figure 21 shows the parameter of Kariuki et al. plotted against the equivalence ratio at lean blowout. While the propane data do indeed produce a parameter near unity—especially at an equivalence ratio over 0.7—the methane data resulted in a parameter value of up to 10.

The data were then run through the Matlab correlation code. To establish a baseline, the initial parameters used were D/U , pressure, and temperature. Equation 21 shows the resulting correlation equation, and the data are plotted in Figure 22. The R-squared value was 0.802. The methane data in Figure 10 clearly do not follow the same trend as the propane data. In addition, it appears that there are two distinct curves within the methane data, each corresponding to a different D/U ratio.

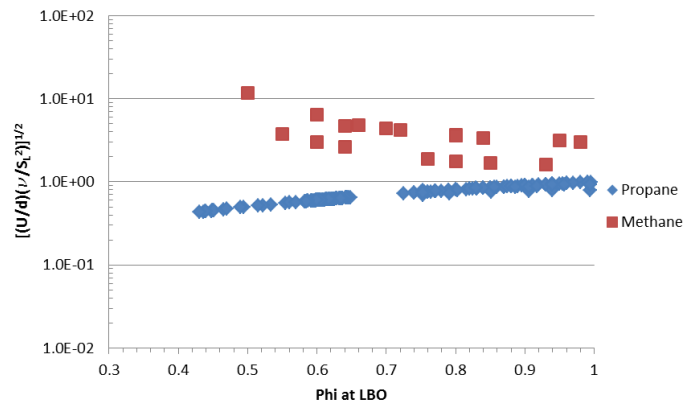


Figure 19. Kariuki Parameter Plotted against Equivalence Ratio at Lean Blowout

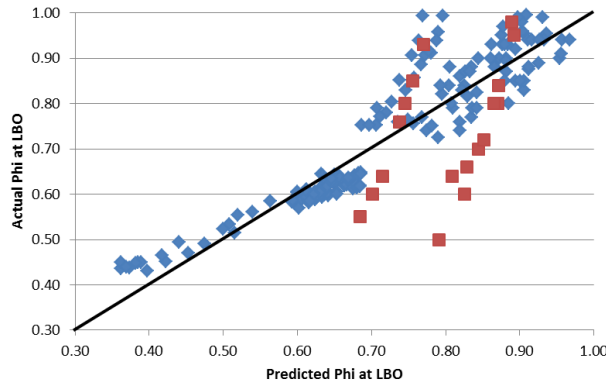


Figure 20. Flame Speed Dataset Correlation Results with D/U , Temperature, and Pressure as Factors ($R^2=0.802$)

$$\phi_{predicted} = \frac{38.95}{\left(\frac{D}{U}\right)^{0.1067} P^{0.3170} T^{0.8586}} \quad (21)$$

Because laminar flame speed has been indicated by previous researchers [9, 10] as a critical parameter in blowout, it was used to replace the pressure and temperature in the correlation as the chemical “timescale.” The resulting correlation equation is Eq 22. Including laminar flame speed improved the R-squared value from 0.802 to 0.846.

$$\phi_{predicted} = \frac{0.9088 \times S_L^{0.3725}}{\left(\frac{D}{U}\right)^{0.0324}} \quad (22)$$

Equation 22 reveals multiple unexpected outcomes. The fluid-dynamic timescale appears to have lost its significance in the blowout process. In addition, the laminar flame speed is in the numerator, suggesting that the higher the laminar flame speed, the less stable the flame—which is in opposition to most physical explanations of flame stability. A more likely explanation emphasizes the need for caution when using correlations to explore physical phenomena in large datasets.

It is very probable that the correlation is not actually predicting lean blowout but rather is creating a laminar flame speed curve. Laminar flame speed increases with equivalence ratio when the flame is lean, as demonstrated previously in Figure 17. The correlation algorithm recognized this and simply correlated the flame speed to the equivalence ratio. If more data were available where the flame speeds differed substantially at the same equivalence ratio, the equivalence ratio/flame speed link might be broken, and the correlation could be run to predict lean blowout. With the current dataset, the laminar flame speed cannot be used to predict blowout.

2.2.3.2 Correlation with Ignition Delay Time

Ignition delay time is another chemical timescale that has been proposed as being critical to the blowout process; therefore, a subset of the data was used to correlate with ignition delay time. The methane and propane dataset used for the laminar flame speed calculations could not be used to study the effect of ignition delay time because of the extremely long ignition delay times at atmospheric pressure and relatively low temperatures (below 600 K). Instead, the dataset chosen for the ignition delay time correlation was composed of data taken on a petroleum-derived JP-8 fuel and a tallow-derived HRJ fuel, which have relatively shorter ignition delay times. The chemical mechanism employed [30] uses surrogate mixtures to model each fuel using varying ratios of n-dodecane, n-decane, iso-octane, and propyl-benzene. The ignition delay time for each of the 40 points in the dataset was calculated based on its inlet conditions using Cantera [29]. Because each of these points was taken on vitiated air, the oxidizer composition was calculated using a Matlab function that relies on combustion chemistry and thermodynamic principles of equilibrium to calculate the chemical make-up of the inlet gases after vitiation. The Matlab least-squares curve-fit function was then used to find the desired correlation.

The correlation was first run using only the inlet conditions to establish a baseline comparison. The data correlate quite well with only the inlet conditions, probably because less variation was

present in the dataset than would be the case with more data points. The pressure varied by only around 0.04 atm, and the temperature ranged from 750 to 910 K. In addition, all points were obtained at the AFRL High Pressure Combustion Research Facility, which eliminated some variability due to facility-related inconsistencies. The correlation data are plotted in Figure 23, and the correlation equation is Eq 23. The R-squared value is 0.942.

$$\phi_{predicted} = \frac{94.59}{\left(\frac{D}{U}\right)^{0.3278} P^{0.8096} T^{1.266}} \quad (23)$$

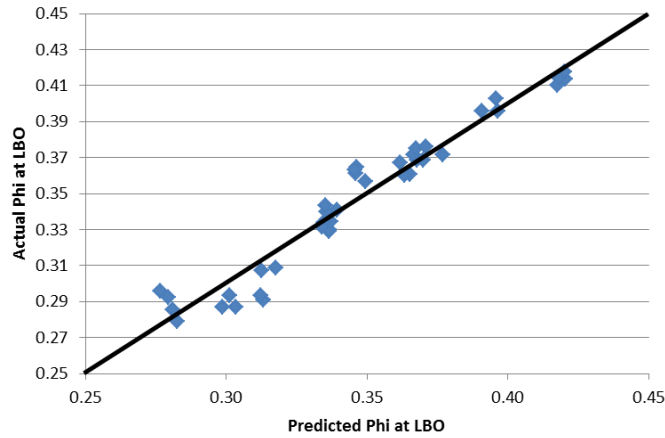


Figure 21. Ignition Delay Dataset Correlation Results with D/U, Temperature, and Pressure as Factors ($R^2=0.942$)

Because both pressure and temperature affect ignition delay time, they were replaced in the next correlation with the ignition delay time (IDT) as shown in Eq 24. The data are plotted in Figure 24. When the ignition delay time was substituted into the correlation, the R-squared value decreased to 0.918. However, the data continues to fall very near the perfect-fit line.

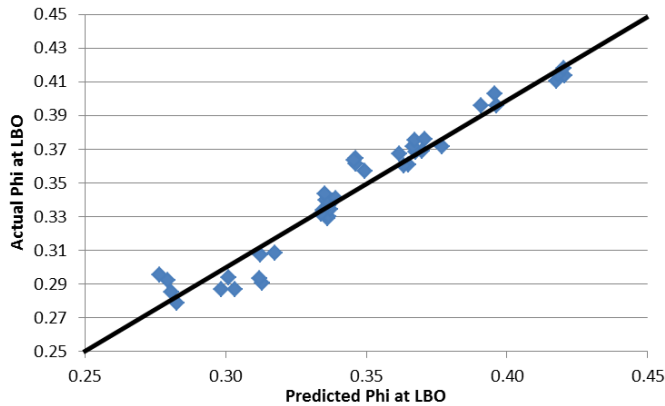


Figure 22. Ignition Delay Dataset Correlation Results with D/U and IDT as Factors ($R^2=0.918$)

$$\phi_{predicted} = \frac{0.0139 \times IDT^{0.0920}}{(D/U)^{0.3183}} \quad (24)$$

To verify that the data were not solely dependent on the fluid-mechanic timescale, the correlation was also run with the D/U parameter only, as shown in Eq 25. This resulted in an R-squared value of 0.381. In addition, the data no longer fell as close to the perfect-fit line, as shown in Figure 25.

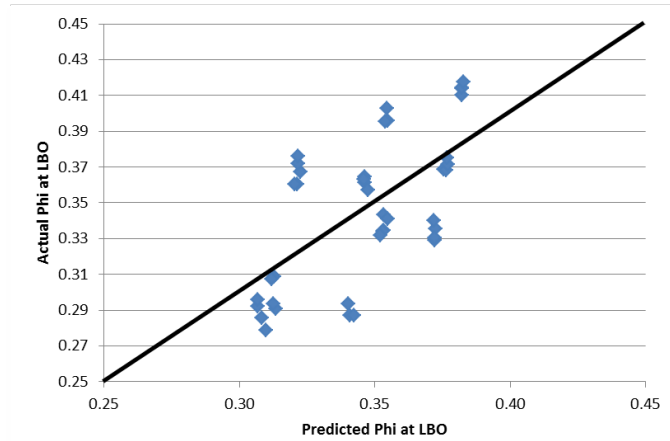


Figure 23. Ignition Delay Dataset Correlation Results with D/U as the Only Factor ($R^2=0.381$)

$$\phi_{predicted} = \frac{0.0286}{(D/U)^{0.3138}} \quad (25)$$

The data are more scattered when no chemical timescale parameters are included. Although the pressure and temperature are adequate to fit the data, they are not direct timescales that can be included in a Damköhler-type number. While ignition delay time appears to be an adequate substitute for this particular dataset, the dataset was relatively small. All points were taken in the High Pressure Combustion Research Facility at AFRL within a fairly small range of inlet conditions and fuel properties. Because the data lack a lot of variation, the correlation does a very good job of predicting blowout without specifically identifying a chemical timescale; therefore, it is difficult to discern whether including ignition delay time would have a more or less significant impact in a larger dataset. However, for the dataset used in this study, the ignition delay time did provide an adequate representation of chemical timescale.

2.2.3.3 Correlation Validation

To assess the accuracy of the correlation, the correlation including hydrogen-to-carbon ratio and oxygen content was used to predict the blowout of bluff-body flames at an additional 47 conditions. The blowout points were selected from propane and jet fuel experiments run in the Atmospheric Pressure Combustion Laboratory at AFRL as well as from propane experiments conducted by Yamaguchi et al. [19]. Figure 14 displays a plot of the validation points, shown in yellow, as well as the points used in the correlation, the equation of which is shown again in Eq 26.

$$\phi_{predicted} = \frac{1.02 \times 10^3}{\left(\frac{D}{U}\right)^{0.1464} P^{0.2612} T^{0.8416} \left(\frac{H}{C}\right)^{0.2130} O_2^{1.131}} \quad (26)$$

The average error of the prediction within the validation dataset was 10.57%. The AFRL propane and jet fuel datasets lie near the perfect-fit line and have an average error of 6.92% and 5.08%, respectively.

The data of Yamaguchi et al. also lie relatively near the perfect-fit line, with the exception of an obvious outlier at an actual blowout of 0.4. This point was also something of an outlier in the original data of Yamaguchi et al [19]. Of particular interest concerning the Yamaguchi data is that flameholder configurations employing multiple bluff bodies were used. The blockage ratio of the experiment was kept constant by changing the flameholder diameter when the number of flameholders was changed [19]. When calculating the predicted equivalence ratio at lean blowout, only the actual diameter of the individual flameholders was taken into account. The correlation predicted the lean blowout of the Yamaguchi points with an average error of 19.54%. If the outlier is excluded, the average error falls to 16.78%.

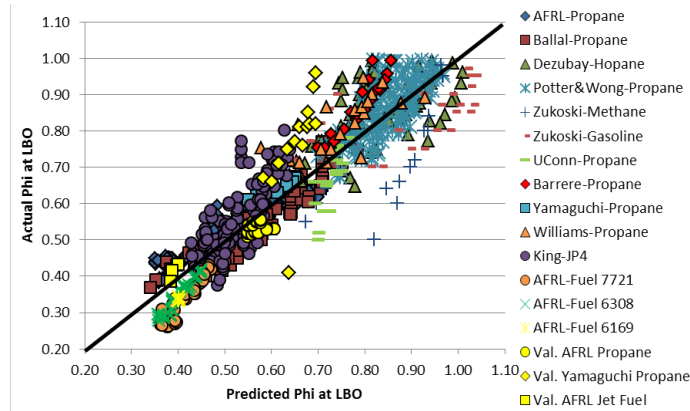


Figure 24. Correlation Results with H/C and Oxygen Content, Showing Validation Points

The average error in the predicted equivalence ratio for all points, including those used to form the correlation equations, was 8.10%. The maximum error was 64.00%, which was the error on a point taken on methane. Methane points were generally associated with higher errors, with an average of 19.88%.

2.2.4 Discussion

Several of the parameters in the correlation shown in Eq 26 are logical extensions of the Damköhler number theories presented in previously published literature. D/U is the fluid mechanic timescale, where U is the lip velocity and D the flameholder diameter. This finding supports the conclusions of many past researchers [5, 8, 12] and implies that the mixing time in the shear layer between the hot products in the recirculation zone and the fresh reactants flowing past the flameholder is an important timescale. As the fresh reactants flow past the recirculation zone, they mix in the shear layer with hot combustion products. If the reactants do not mix and react sufficiently in the amount of time that they spend in the shear layer, the flame cannot propagate. Because the dimensions of the recirculation zone generally scale with the width of

the flameholder, the width of the flameholder can be substituted for the recirculation zone length, although it introduces some variability to the correlation.

Both pressure and temperature contribute to the chemical timescale in the Damköhler number. In the correlation equation shown in Eq. 26, the equivalence ratio at lean blowout decreases as the pressure and temperature increase. In general, as the pressure and temperature of a combustible mixture increase, the reactivity of that mixture increases. If the reactivity of the mixture in a bluff-body flame increases, the chemical timescale should decrease, resulting in a flame that should be able to propagate in more adverse flow conditions.

For this dataset, the molecular weight appears to have a minimal effect on the equivalence ratio at lean blowout. However, the hydrogen-to-carbon ratio does improve the correlation. The hydrogen-to-carbon ratio is, to some extent, an indication of the tendency of the fuel to ignite, or its cetane number. The cetane number of chemical components typically present in jet fuels shows the following trend: normal alkanes > branched alkanes > cycloalkanes > aromatics [27]. As demonstrated in Table 4, the hydrogen-to-carbon ratio of these structures follows a similar trend and, therefore, is an indicator of the relative ignition time of the fuel. If the ignition delay time is an adequate representation of the critical chemical timescale in the Damköhler number, then it logically follows that the cetane number—and, therefore, the hydrogen-to-carbon ratio—would have an influence in the correlation for jet fuels.

Table 4. Hydrocarbon Structures and Their Relative Cetane Numbers and H/C Ratios

Increasing Cetane Number	Hydrocarbon	General formula	Example molecule	H/C ratio
	Normal alkanes	$C_n H_{2n+2}$	Hexane (C_6H_{14})	2.33
	Branched alkanes	$C_n H_{2n+2}$	Iso-hexane (C_6H_{14})	2.33
	Cycloalkanes	Dependent	Cylco-hexane	2
	Aromatics	Varies	Benzene (C_6H_6)	1

A relationship between cetane number and lean blowout was also found by Colket et al. [28] who used experimental combustor data taken with a variety of jet fuels. They found that fuels with higher cetane numbers blew out at lower equivalence ratios, as shown in Figure 27. In addition, they found that fuels with more n-alkanes, which have high hydrogen-to-carbon ratios, are less likely to blow out.

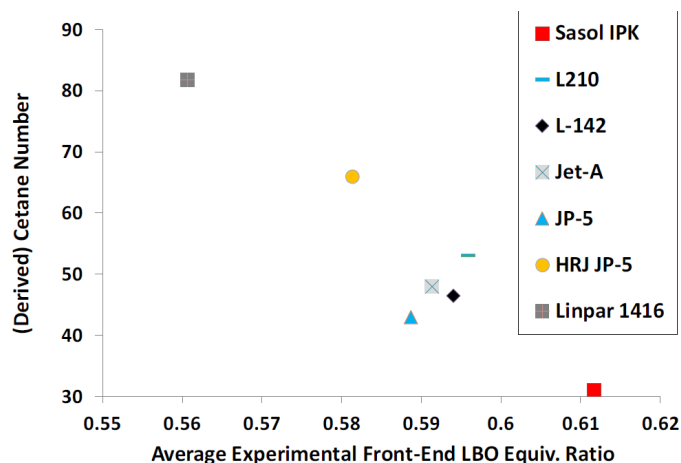


Figure 25. Derived Cetane Number against Equivalence Ratio at LBO ^[28]

In the correlation shown in Eq 14, the hydrogen-to-carbon ratio is in the denominator, which implies that the higher the hydrogen-to-carbon ratio, the more resistant the flame is to lean blowout. In jet fuels, a higher hydrogen-to-carbon ratio indicates more n-alkanes and a higher cetane number; therefore, a more stable flame would indeed be anticipated.

The last parameter included in Eq 26 is the oxygen concentration of the incoming air after vitiation. Less oxygen content in the air should lengthen the chemical timescales involved and, thereby, increase the equivalence ratio at lean blowout. This behavior is confirmed by the presence of the oxygen content in the denominator of Eq 26.

2.2.5 Conclusions

Lean blowout data was collected on propane and jet fuel bluff-body stabilized flames and was combined with data taken from past literature to create a database of over 1100 data points. Cantera was used to calculate the laminar flame speeds for 200 data points taken on propane and methane over a range of pressures, temperatures, velocities, Reynolds numbers, and flameholder geometries. Ignition delay times were also calculated for 40 data points taken on conventional and alternative jet fuels. A least-squares curve-fit algorithm was run using Matlab to find a correlation that could accurately predict the equivalence ratio at lean blowout for each dataset.

The best correlation for the overall dataset included pressure, temperature, the ratio of flameholder diameter to lip velocity, oxygen level, and the hydrogen-to-carbon ratio of the fuel as factors. The R-squared value of this correlation was 0.873. The exponents on the factors indicated that high pressure and temperature lowered the equivalence ratio at lean blowout, as did high levels of oxygen. These factors contribute to the chemical timescale in the Damköhler number. The correlation also indicated that the equivalence ratio at lean blowout decreases as the hydrogen-to-carbon ratio increases. In jet fuels, high hydrogen-to-carbon ratios indicate increased levels of alkanes, which have higher cetane numbers and shorter ignition delay times. The ratio of flameholder diameter to lip velocity is recognized as the fluid mechanic timescale in the Damköhler number.

The correlation for the ignition delay dataset with pressure, temperature, and the ratio of flameholder diameter to lip velocity as factors had an R-squared value of 0.942. This relatively

small, uniform dataset correlates very well. When ignition delay time replaces pressure and temperature, the data continues to correlate well, with an R-squared value of 0.918. For this limited dataset, the ignition delay time is an adequate representation of the chemical timescale.

2.2.6 References

- [1] Williams, G. C., 1949, "Basic Studies on Flame Stabilization," Fourth National Flight Propulsion Meeting, I.A.S., Cleveland, Ohio, March 18.
- [2] DeZubay, E. A., 1950, "Characteristics of Disk-Controlled Flame," *Aero Digest* **61**, pp. 54-56, 102-104.
- [3] King, C. R., 1957, "Experimental Investigation of Effects of Combustion Chamber Length and Inlet Total Temperature, Total Pressure, and Velocity on Afterburner Performance," NACA RM-E57CO7, Lewis Flight Propulsion Laboratory, Cleveland, Ohio, June 3.
- [4] Zukoski, E. E., 1954, "Flame Stabilization on Bluff Bodies at Low and Intermediate Reynolds Numbers," PhD Dissertation, California Institute of Technology, Pasadena, California.
- [5] Zukoski, E. E., and Marble, F. E., 1955, "Experiments Concerning the Mechanism of Flame Blowoff from Bluff Bodies," Proceedings of the Gas Dynamics Symposium on Aerothermochemistry, Northwestern University, Evanston, Illinois.
- [6] Ozawa, R. I., 1971, "Survey of Basic Data on Flame Stabilization and Propagation for High Speed Combustion Systems," AFAPL-TR-70-81, Air Force Aero Propulsion Laboratory, Wright-Patterson Air Force Base, Ohio.
- [7] Ballal, D. R., and Lefebvre, A. H., 1979, "Weak Extinction Limits for Flowing Turbulent Mixtures," *Journal of Engineering for Power* **101**, pp. 343-348.
- [8] Plee, S. L., and Mellor, A. M., 1979, "Characteristic Time Correlation for Lean Blowoff of Bluff-Body-Stabilized Flames," *Combustion and Flame* **35**, pp. 61-80.
- [9] Radhakrishnan, K., Heywood, J. B., and Tabaczynski, R. J., 1981, "Premixed Turbulent Flame Blowoff Velocity Correlation Based on Coherent Structures in Turbulent Flows," *Combustion and Flame* **42**, pp. 19-33.
- [10] Kariuki, J., Cavaliere, D. E., Letty, C., and Mastorakos, E., 2012, "A Comparison of the Blow-off Behaviour of Swirl-Stabilized Premixed and Spray Flames," 50th AIAA Aerospace Sciences Meeting, Nashville, Tennessee, January 9-12.
- [11] Nair, S., and Lieuwen, T., 2007, "Near-Blowoff Dynamics of a Bluff-Body Stabilized Flame," *Journal of Propulsion and Power* **23**, pp. 421-427.
- [12] Husain, S. A., 2008, "Analysis of Blowoff Scaling of Bluff Body Stabilized Flames," MS Thesis, Georgia Institute of Technology, Atlanta, Georgia.
- [13] Shanbhogue, S. J., Husain, S., and Lieuwen, T., 2009, "Lean blowoff of Bluff Body Stabilized Flames: Scaling and Dynamics," *Progress in Energy and Combustion Science* **35**, pp. 98-120.
- [14] Chaudhuri, S., Kostka, S., Tuttle, S. G., Renfro, M. W., and Cetegen, B. M., 2011, "Blowoff Mechanism of Two Dimensional Bluff-Body Stabilized Turbulent Premixed Flames in a Prototypical Combustor," *Combustion and Flame* **158**, pp. 1358-1371.
- [15] Khosla, S., Leach, T., and Smith, C., 2007, "Flame Stabilization and Role of von Karman Vortex Shedding Behind Bluff Body Flameholders," 43rd AIAA/ASME/SAE/ASEE Joint Propulsion Conference and Exhibit, Cincinnati, Ohio, July 8-11.
- [16] Huelskamp, B. C., Kiel, B. V., Lynch, A. C., Kostka, S., Gokulakrishnan, P., and Klassen, M., 2011, "Improved Correlation for Blowout of Bluff Body Stabilized Flames," 49th AIAA Aerospace Sciences Meeting, Orlando, Florida, January 4-7.
- [17] Won, S. H., Veloo, P. S., Santner, J., Ju, Y., and Dryer, F. L., "Comparative Evaluation of Global Combustion Properties of Alternative Jet Fuels," 2013, 51st AIAA Aerospace Sciences Meeting, Grapevine, Texas, January 7-10.
- [18] Potter, A. E., and Wong, E. L., 1958, "Effect of Pressure and Duct Geometry on Bluff-Body Flame Stabilization," NACA TN-4381, Lewis Flight Propulsion Laboratory, Cleveland, Ohio.
- [19] Yamaguchi, S., Ohiwa, N., and Hasegawa, T., 1985, "Structure and Blow-Off Mechanism of Rod-Stabilized Premixed Flame," *Combustion and Flame* **62**, pp. 31-41.
- [20] Barrère, M., and Mestre, A., 1954, "Stabilisation Des Flamme Par Des Obstacles," *Selected Combustion Problems: Fundamentals and Aeronautical Applications*, North Atlantic Treaty Organization, Advisory Group on Aeronautical Research and Development, pp. 426-446.
- [21] Montgomery, D. C., and Runger, G. C., 2006, *Applied Statistics and Probability for Engineers*. New York: Wiley. Chap. 10.
- [22] Smith, G. P., Golden, D. M., Frenklach, M., Moriarty, N. W., Eiteneer, B., Goldenberg, M., Bowman, C. T., Hanson, R. K., Song, S., Gardiner, W. C., Lissianski, V. V., and Qin, Z., "GRI-Mech 3.0," http://www.me.berkeley.edu/gri_mech/
- [23] Gokulakrishnan, P., Fuller, C. C., Klassen, M. S., Joklik, R. G., Kochar, Y. N., Vaden, S. N., Lieuwen, T. C., and Seitzman, J. M., 2014, "Experiments and Modeling of Propane Combustion with Vitiating," *Combustion and Flame* **161**, pp. 2038-2053.
- [24] Dooley, S., Won, S. H., Chaos, M., Heyne, J., Ju, Y., Dryer, F. L., Kumar, K., Sung, C. J., Wang, H., Oehlschlaeger, M. A., Santoro, R. J., and Litzinger, T. A., 2010, "A Jet Fuel Surrogate Formulated by Real Fuel Properties," *Combustion and Flame* **157**, pp. 2333-2339.

- [25] Dooley, S., Won, S. H., Jahangirian, S., Ju, Y., Dryer, F. L., Wang, H., and Oehlschlaeger, M. A., 2012, "The Combustion Kinetics of a Synthetic Paraffinic Jet Aviation Fuel and a Fundamentally Formulated, Experimentally Validated Surrogate Fuel," *Combustion and Flame* **159**, pp. 3014-3020.
- [26] Smith, C. E., Nickolaus, D., Leach, T., Kiel, B., and Garwick, K., 2007, "LES Blowout Analysis of Premixed Flow Past V-gutter Flameholder," 45th AIAA Aerospace Sciences Meeting, Reno, Nevada, January 8-11.
- [27] Totten, G. E., Westbrook, S.R., and Shah, R. J., 2003, *Fuels and Lubricants Handbook: Technology, Properties, Performance, and Testing*, West Conshohocken, Pennsylvania: ASTM International, pp. 118-120.
- [28] Colket, M., Zeppieri, S., Dai, Z., and Hautman, D., 2012, "Fuel Research at UTRC," Multi-Agency Coordinating Council for Combustion Research 5th Annual Fuel Research Meeting, Livermore, California, September 17-20.
- [29] Goodwin, 2009, "Cantera: An Object-Oriented Software Toolkit for Chemical Kinetics, Thermodynamics, and Transport Processes," Caltech, Pasadena, California. <http://code.google.com/p/cantera>.
- [30] Gokulakrishnan, P., Fuller, C. C., Klassen, M. S. and Kiel, B. V., 2014, " Ignition Characteristics of Alternative JP-8 and Surrogate Fuels under Vitiated Conditions", 50th AIAA Joint Propulsion Conference, Cleveland, OH, AIAA 2014-3664